AN ABSTRACT OF THE THESIS OF

Kristal Williams for the degree of Master of Science in Water Resources Engineering presented on June 3, 2019.

Title: The Effect of Flowrate on Trapping in a Two-phase System as it Relates to CO_2 Sequestration

Abstract approved: _____

Dorthe Wildenschild

This research examines the independent and combined effects of drainage and imbibition flowrate on nonwetting phase capillary trapping in a two-phase, porous medium system. A uniform system of cubic arrangement and non-uniform systems of both cubic and rhombohedral arrangements were examined in order to analyze and compare the nonwetting phase trapping trends between uniform and non-uniform porous media. The unique system set-up, composed of similar refractive indexes of the wetting phase and medium, allows flow experiments to be performed in 3-D printed bead packs (of different arrangements) (44.8x44.8x2.8mm) and quantified with 2-D images. All beads are 700µm in diameter, comparable to the grain size of a sandstone. Soltrol and water (proxy fluids for brine and supercritical CO_2) were used in flow experiments. For the uniform cubic arrangement, it was found that slower drainage flowrates, regardless of the subsequent imbibition flowrate, resulted in the largest amount of nonwetting phase trapped in comparison to higher drainage flowrates. Slow drainages correspond to a capillary dominated flow regime and greater disconnect of the nonwetting phase post-drainage, both of which are found to be conducive to nonwetting phase trapping. However, increasing non-uniformity (or the introduction of high porosity zones) in a cubic bead pack was observed to alter

this trend, while trends determined by the uniform cubic arrangement were also observed on the non-uniform rhombohedral bead pack. It is therefore suggested that drainage flowrate ($scCO_2$ injection) and a system's uniformity (formation heterogeneity) be considered in order to favorably influence trapping efficiency in $scCO_2$ injection schemes.

The Effect of Flowrate on Trapping in a Two-phase System as it Relates to CO_2 Sequestration

by
Kristal Williams

A THESIS

submitted to

Oregon State University

in partial fulfillment of
the requirements for the
degree of

Master of Science

Presented June 3, 2019
Commencement June 2019

Master of Science thesis of Kristal Williams presented on June 3, 2019.

APPROVED:

Major Professor, representing Water Resources Engineering

Director of the Water Resources Graduate Program

Dean of the Graduate School

I understand that my thesis will become part of the permanent collection of Oregon State University libraries. My signature below authorizes release of my thesis to any reader upon request.

Kristal Williams, Author

ACKNOWLEDGEMENTS

The author expresses sincere appreciation to Dorthe Wildenschild, for her guidance, expertise, and encouragement; and to her family and friends, for their endless love and support.

TABLE OF CONTENTS

TABLE OF CONTENTS (Continued)

Page

LIST OF FIGURES

Figure Page

LIST OF FIGURES (Continued)

Figure Page

LIST OF FIGURES (Continued)

Figure Page

LIST OF TABLES

Chapter 1: Introduction

Anthropogenic carbon dioxide (CO_2) is currently being released to the atmosphere at a rate faster than natural sinks can remove it. Increasing amounts of atmospheric CO_2 is primarily a result of burning fossil fuels for energy. The burning of fossil fuels as an energy source is expected to continue throughout the century due to both the price and availability (IPCC, 2005).

The massive amount of CO_2 and other greenhouse gases produced in the burning of fossil fuels are changing the optical properties of our atmosphere, resulting in an increasing amount of longwave radiation that is re-radiated back to the Earth's surface. This increase is impacting global temperature and precipitation, and has caused an approximately 1°C of warming in 2017 since pre-industrial times (Allen et al., 2018). This trend is expected to continue if substantial action to reduce atmospheric greenhouse gas concentration is not taken (Garcia et al., 2010).

A potential avenue for reducing the amount of CO_2 in our atmosphere, and/or limiting future emissions, is through capturing CO_2 for long-term storage in deep saline aquifers. CO_2 capture techniques consist of both direct capture from point source emissions, post-combustion (e.g. Leung et al., 2014) and more recent direct-air-capture techniques (e.g. Wilcox et al., 2017). Developing direct-air-capture technologies, remove previously emitted CO_2 from the air to then be processed for subsurface storage. Storage of CO_2 in deep formations is ideal due to the large potential storage capacity. 10,000 Gt of CO_2 is the potential estimated storage capacity of these formations (IPCC, 2005). CO_2 can be stored by taking advantage of capillary trapping, to prevent upward migration of the CO_2 into groundwater reservoirs, in these deep saline aquifers. Injection and capillary trapping of CO_2 in subsurface formations occurs around 800 meters. At this depth

CO_2 is a supercritical fluid ($scCO_2$), as opposed to a vapor (Figure 1). This behavior must be considered in laboratory experiments.

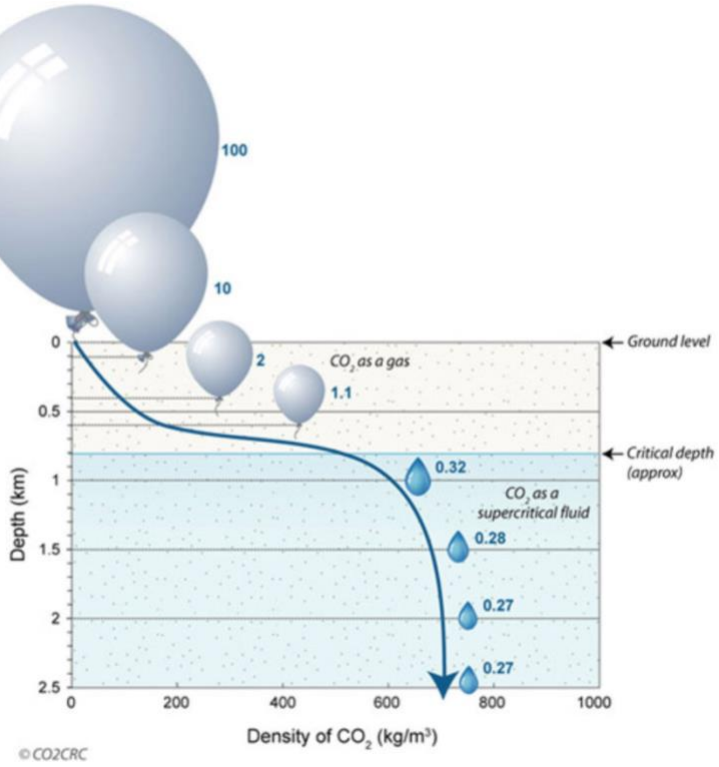

Figure 1: CO_2 phase change with depth. Critical depth at approximately 800m. Wilson et al. (2016)

Subsurface capillary trapping of $scCO_2$ is among four trapping mechanisms, namely structural, capillary (or residual), solubility, and mineralization (Figure 2). CO_2 trapping mechanisms are a function of physical and geochemical processes. Injected $scCO_2$ will dissolve into brine present in the reservoir, known as solubility trapping. It will then eventually precipitate to form stable carbonate minerals, the process known as mineral trapping. Both solubility and mineral trapping occur on the timescale of hundreds to thousands of years (Figure 2). Capillary (or residual) trapping is considered a more reliant mechanism compared to structural trapping. Capillary

trapping traps injected $scCO_2$ within the pore spaces of the reservoir and occurs at relatively shorter timescales. Structural trapping is the trapping of injected $scCO_2$ via the reliance of a low permeability caprock (IPCC, 2005).

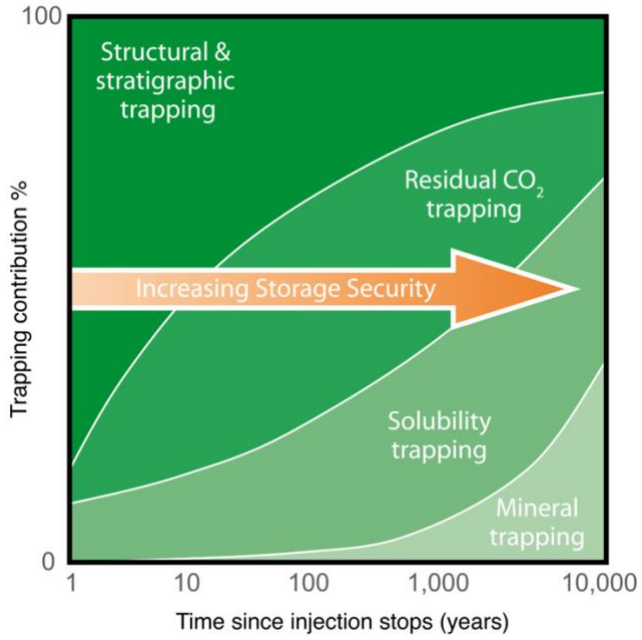

Figure 2: Storage mechanisms of injected scCO2. (IPCC, 2005)

Given the interest in CO_2 sequestration in deep saline aquifers there is interest in improving current understanding of the processes involved. This project investigates the independent and combined effects of drainage and imbibition flowrate on nonwetting phase capillary trapping in two-phase, porous media systems.

Chapter 2: Background

2.1 Fluids in porous media

Porous media, in this work, refers to subsurface formations that contain void spaces known as pores. These formations can store and transmit fluids within their porous network. Common subsurface fluids include water, brine, oil, and contaminants.

When two immiscible (or non-mixing) fluids are present simultaneously in a porous medium, the medium will have a higher affinity or attraction to one fluid over the other. This attraction is referred to as wettability and is system dependent. In a two-phase system, the fluid or phase that the media holds the higher affinity for is referred to as the wetting phase. While the fluid or phase that the media holds the lesser affinity for is referred to as the nonwetting phase for that particular immiscible, two-phase system (Figure 3).

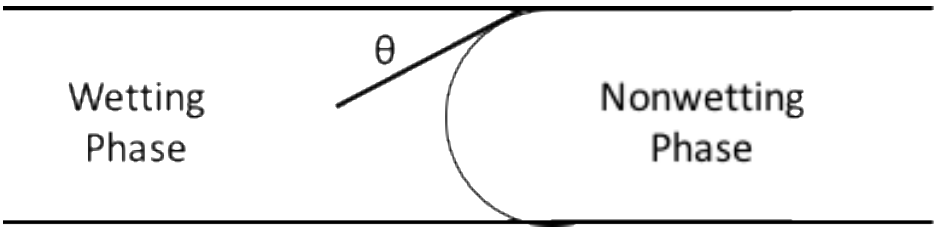

Figure 3: Image of immiscible fluids in a capillary tube. Wetting and nonwetting phase refers to the surfaces attraction to one fluid over the other. The contact angle, θ, quantifies the strength of attraction.

The transmission of fluid through a medium is highly dependent on the wettability. Wettability can occur in varying degrees (or strengths), which is measured by the contact angle between the wetting phase and the solid surface (Figure 3). In a two-phase system, where water is the wetting phase, contact angles measured through the wetting phase between 0° and 65° to 70° are

considered water-wet, between 180° and 105° to 120° are referred to as non-water-wet, and values in between these ranges are considered neutrally wet (Anderson, 1987).

In this work, immiscible proxy-fluids are used to mimic the $scCO_2$-brine immiscible fluid pair. The use of proxy-fluids allows for more efficient experiments and avoids the need for high pressure and temperature set-ups.

2.2 Capillary pressure

In a two-phase, porous medium system, fluid interaction is characterized by capillary pressure. Capillary pressure (P_c) is the difference in pressure between the nonwetting phase (P_{NW}) and the wetting (P_W), as defined below:

$$P_c = P_{NW} - P_W$$

Equation 1

Using the Young-Laplace equation, capillary pressure can be determined using the interfacial tension between the two immiscible fluids, σ, the contact angle which forms on the capillary tube's surface, θ, and the radius of the capillary tube, r:

$$P_c = \frac{2\sigma \cos\theta}{r}$$

Equation 2

When the contact angle is at or near 0° (indicating a strongly wetted system) Equation 2 is reduced to:

$$P_c = \frac{2\sigma}{r}$$

Equation 3

2.3 Drainage and Imbibition

Drainage and Imbibition refer to the characteristic flow events in porous media. In a two-phase porous system, drainage refers to the nonwetting phase displacing the wetting phase. Imbibition refers to the wetting phase displacing the nonwetting phase.

Experiments described here consists of an initial imbibition event and subsequent drainage and imbibition events, referred to as primary imbibition, primary drainage, and secondary imbibition. Primary imbibition is the flow event that saturates dry porous media with the wetting phase. As the wetting phase invades the pore space of the media and saturation is achieved, hydrostatic pressure becomes zero. This state resembles a brine-saturated aquifer at a scCO_2 sequestration site before CO_2 is injected. Primary drainage introduces the nonwetting phase into the system by allowing the nonwetting phase to displace the wetting phase. The nonwetting phase will never fully displace the wetting phase; there will remain an irreducible amount of wetting phase (S_{irr}) within the system (Figure 5). This process resembles CO_2 injection into an aquifer. Secondary imbibition is the flow event that floods the system again with the wetting phase, this time trapping a portion of the nonwetting phase that was introduced during primary drainage within the pore spaces. This process resembles the trapping of CO_2 within the porous media of the aquifer due to the subsequent flooding event.

2.4 Capillary Pressure Saturation Curve

A capillary pressure saturation curve is typically used to characterize two-phase flow within porous media. It relates the saturation of the systems wetting phase and the pressures required to drain or flood the system. Wetting phase saturation (S_W) is defined as:

$$S_W = \frac{\text{Volume of wetting phase}}{\text{Total pore volume}}$$

Equation 4

During drainage, pressures are increased until the capillary pressure needed to drain the first pore neck is reached. During the imbibition cycle, pressure decreases until the capillary pressure needed to fill the first pore body is reached, Equation 3 (Figure 4) (Dullien, 1992). Following the emptying or filling of the first pore neck or body, the system continues to drain or fill, increasing or reducing pressure, as is shown in Figure 5. At the completion of drainage, an irreducible amount of the wetting phase will remain in the system, referred to as S_{irr}. At the completion of imbibition, a residual amount of the nonwetting phase will remain in the system, this is considered the trapped nonwetting phase.

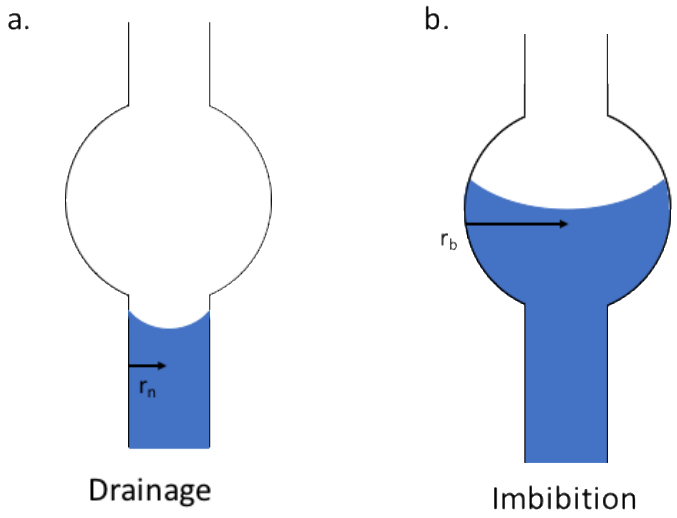

Figure 4: a.) Capillary pressure during drainage is dependent on pore neck radius, r_n. b.) Capillary pressure during imbibition is dependent on pore body radius, r_b.

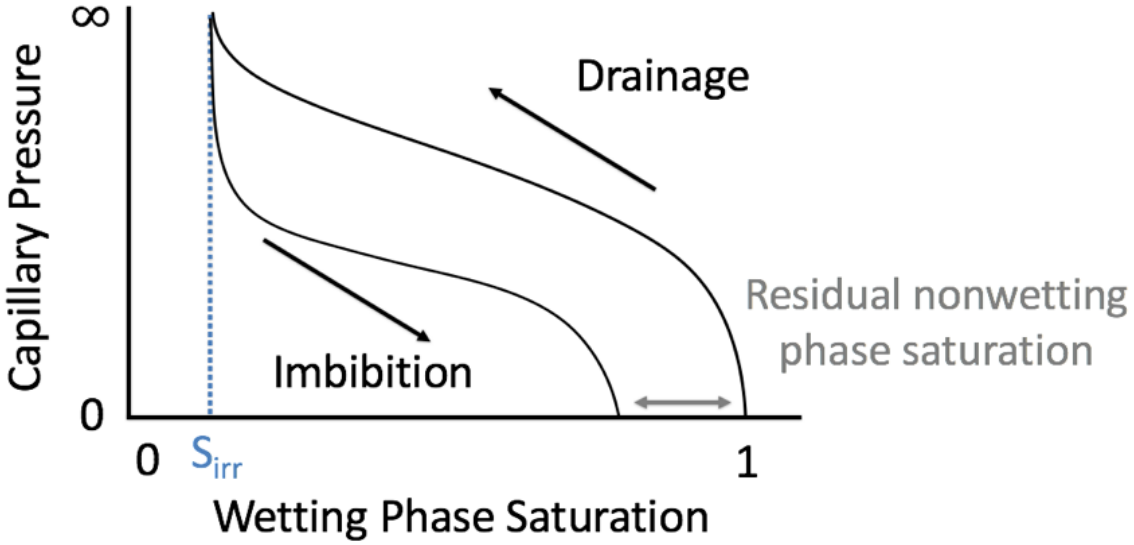

Figure 5: Capillary pressure saturation curve, wetting phase saturation (S_w) and capillary pressure. Hysteresis in this system (due to the difference in pressures required for drainage and imbibition to occur) results in a residual amount of nonwetting phase saturation after drainage and imbibition cycles.

Hysteresis in this system is due to pore structure effects and is the misalignment of the drainage and imbibition phase on the capillary pressure saturation curve, as a result of the difference in capillary pressures required for imbibition and drainage to occur (Figure 5).

2.5 Flow predictors

In two-phase, porous media systems, typical flow predictors are Capillary number, Mobility ratio, and Bond number. These quantify the interplay of a system's fluid properties, media properties, and flowrate.

2.5.1 Capillary Number

Capillary number (C_a) is the ratio of viscous forces to capillary forces, defined as:

$$Ca = \frac{\text{Viscous force}}{\text{Capillary force}} = \frac{\mu_{inv}\, V_{inv}}{\sigma}$$

Equation 5

μ_{inv} is the viscosity of the invading fluid, σ is the interfacial tension between the two fluids, V_{inv}, is the velocity of the invading fluid defined as:

$$V = \frac{Q\,[\frac{m^3}{s}]}{A\,[m^2] \varnothing\,[-]}$$

Equation 6

where Q is the volumetric flowrate (the rate the pump is operating at in this case), A is the cross-sectional area of the porous media, and $\varnothing$ is the porosity of the system (Chatzis and Morrow, 1984).

2.5.2 Mobility Ratio

Mobility ratio (M) is defined as:

$$M = \frac{\mu_{inv}}{\mu_d}$$

Equation 7

where μ_{inv} is the viscosity of the invading fluid (wetting phase during imbibition and nonwetting phase during drainage) and μ_d is the viscosity of the displaced fluid (nonwetting phase during imbibition and wetting phase during drainage) (Lenormand et al., 1988; Zhang et al., 2011). The capillary number and mobility ratio are used as predictors for determining the force that will dominate the fluid flow in a two-phase system, when placed on what is often referred to as a Lenormand diagram.

2.5.3 Gravity

Due to the properties of the fluid pair presented in this work and in order to isolate the effects of flowrate, gravity effects were not considered in the analysis by removing the impact of gravity and performing horizontal flow experiments.

2.6 Quantitative measures

2.6.1 Saturation of the nonwetting phase

Saturation of the nonwetting phase refers to the amount of nonwetting phase present in a system, quantified by the fraction of pore volume filled with nonwetting phase. Saturation can more specifically reference the amount of nonwetting phase present after drainage and imbibition, referred to as initial saturation (S_I) and residual saturation (S_r). Initial saturation (S_I) of the nonwetting phase refers to the amount of nonwetting phase present after drainage, while, residual saturation (S_r) of the nonwetting phase refers to the amount of nonwetting phase present (or trapped via capillary trapping) after drainage and imbibition. The trapping efficiency after both drainage and imbibition is referred to as residual saturation (S_r) over initial saturation (S_I), or (S_r/ S_I).

2.6.2 Topology of the nonwetting phase

Topology refers to the connectivity (or connectedness) of a phase. The Euler number (χ) is used to quantify topology of the nonwetting phase, defined as:

$$\chi = \beta_0 - \beta_1 + \beta_2$$

Equation 8

Where β_0 , β_1 , and β_2 are referred to as Betti numbers. The zeroth Betti number (β_0) refers to the number of distinct fluid elements in the system, the first Betti number (β_1) refers to the number of redundant connections in the structure of each fluid element, and the second Betti

number (β_2) refers to the number of enclosed voids in the fluid element (Herring et al., 2013) (Figure 6).

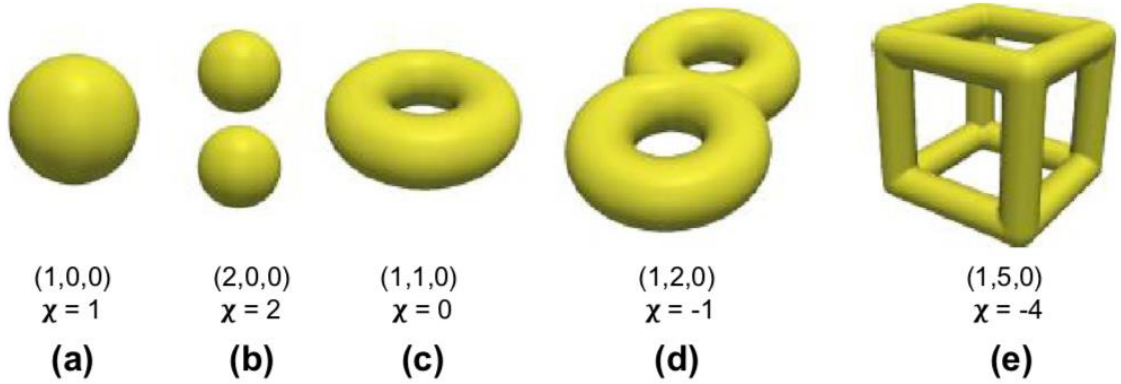

Figure 6: Example Betti numbers (β_0 , β_1 , and β_2) and Euler number (χ) for solid objects. (Herring et al., 2013) adapted from (Wildenschild and Sheppard 2013).

Due to the pseudo-3-D nature of the system presented in this work, there is assumed to be no concavities or voids ($\beta_2 = 0$). The Euler number is therefore simplified to:

$$\chi = \beta_0 - \beta_1$$

Equation 9

A larger Euler number corresponds to a more disconnected system, while a more negative Euler number corresponds to a more interconnected system (Figure 6).

2.7 Index of Refraction

Index of refraction refers to the way light propagates through a medium, represented by a dimensionless number. When two materials have a similar refractive index, light passes through the materials in a similar way and visual distinction is difficult.

In this work, similar refractive indices of both the medium and wetting phase are achieved. These similarly appearing phases are paired with a high-contrasting nonwetting phase. This allows the medium and wetting phase to appear as one phase, and for the nonwetting phase to be easily distinguished from the two. This distinction provides the ability to easily quantify the amount of trapped nonwetting phase in the three-dimensional system with a two-dimensional image.

2.8 Imaging

In this work, two-dimensional images were collected using a Canon EOS Rebel T5i. The use of refractive index matching of the wetting phase and the medium coupled with the high-contrasting nonwetting phase, allows for more efficient experiments and avoids the need for complex 3-D imaging technique (e.g. Wildenschild and Sheppard 2013).

Chapter 3: Literature Review

Two-phase fluid flow in porous media and capillary trapping of the nonwetting phase, as it relates to CO_2 sequestration, has been extensively studied. This section will discuss the current understanding of flow through porous media as it relates to residual nonwetting phase trapping, considering dominating forces, snap-off phenomena, flowrate, topology, and experimental designs. The literature referenced in this section largely consists of two-dimensional (2-D) micromodel studies and three-dimensional (3-D) flow experiments. These studies utilize immiscible fluid flow experiments that are readily related to the work presented. Relevant oil-recovery literature is also included in this section. It is important to note that oil-recovery is a similar, reversed process relative to $scCO_2$ sequestration. The goal of oil-recovery is to extract the largest amount of nonwetting phase (oil), while the concern of $scCO_2$ sequestration is to trap the greatest amount of nonwetting phase ($scCO_2$). Further, both the drainage and imbibition phases can be engineered in $scCO_2$ sequestration, while oil-recovery is limited to engineering the imbibition phase, as oil is already present in the subsurface. Lastly, some relevant model literature is included in this section. All studies presented are specified as being either 2-D flow experiment, 3-D flow experiment, oil-recovery, or a model to assist with clarity.

To our knowledge, no previous work has studied the impact of alteration of flowrates on both the drainage and secondary imbibition phase in a single experiment.

3.1 Dominating forces

Previous work conducted in 2-D micromodels has determined that distinct regions dominated by capillary, viscous, or stable displacement forces can be identified, for the drainage process, within

a particular system on a Lenormand diagram, which plots the log of experimental mobility ratio against the log of experimental capillary number (Figure 7) (Lenormand et al., 1988; Zhang et al., 2011). These regions are characterized by distinct flow regimes or fluid flow patterns, Figure 8. In the capillary fingering region, which is a result of low capillary numbers, viscous forces are negligible and capillarity dominates. In the viscous fingering region, viscosity of the displaced fluid is the driving force. In the stable displacement region, viscosity of the injection fluid is the controlling force (Lenormand et al., 1988).

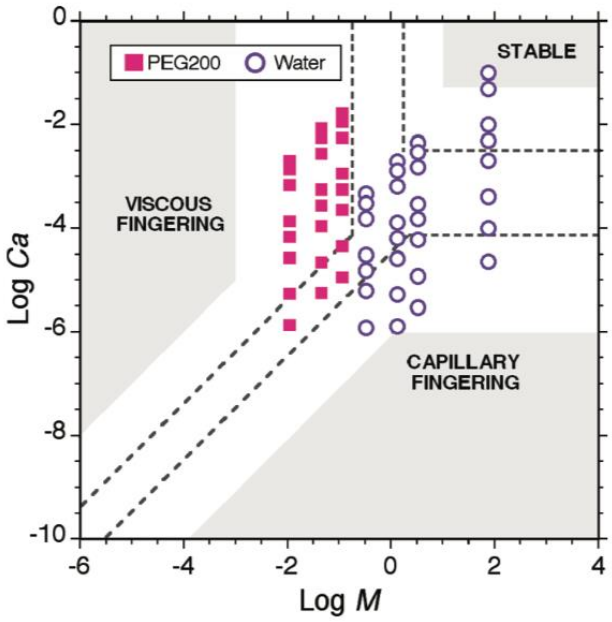

Figure 7: Log Ca-log M force dominating boundaries. Boundaries are system-dependent. Grey shaded region displayed stable regions indicated by Lenormand et al., 1988. Black dashed lines display stable regions indicated by Zhang. (Zhang et al., 2011)

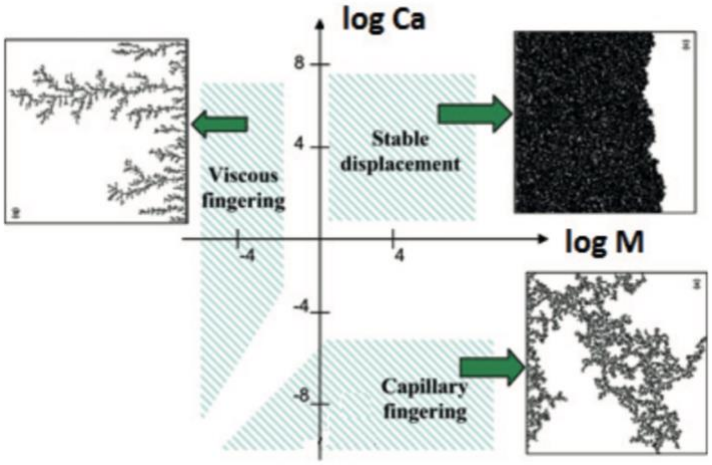

Figure 8: Lenormand phase diagram and corresponding flow regimes. (Knapik et al., 2015)

Capillary number and mobility ratio, as defined in Equation 5 and 7, include fluid viscosity, interfacial tension, and experimental velocity. The utilization of a force dominating diagram and understanding how the capillary number, mobility ratio, and corresponding parameters influence an experimental placement on such diagram, allows for experiments to be conducted and controlled in new systems.

3.2 Snap-off

Snap-off is a phenomenon that occurs as the nonwetting phase makes its way through a wetting phase lined pore. Additionally, the fluid interface (nonwetting and wetting) must pass the wetting phase lined pore by a distance of several throat radii before the appropriate pressures are obtained in order for snap-off to occur (Roof, 1970). Nguyen et al. (2006) used a dynamic model and showed snap-off to be influential in nonwetting phase trapping and favored by a slow displacement rate and small contact angle, sensitivity of snap-off to displacement rate and contact angle is dependent on pore-throat aspect ratio. Pore-throat aspect ratio is the ratio of pore and throat size, a high aspect ratio relates to large pores and small throats.

3.3 Flowrate

Previous work has analyzed the influence of capillary number parameters on residual nonwetting phase trapping (Bachu and Bennion, 2008; Morrow et al., 1988). The experimental capillary number is composed of fluid properties and engineering parameters, viscosity, interfacial tension, and velocity (Equation 5). The significance of velocity or experimental flowrate on trapping of the nonwetting phase, as it relates to CO_2 sequestration, has presented with conflicting results.

Herring et al. (2013), studied both the initial nonwetting (post-drainage) fluid topology and the residual trapping of the nonwetting phase within Bentheimer sandstone cores. Determining that maximum trapping in the Bentheimer sandstone cores is influenced by post-drainage connectivity of the nonwetting phase and the imbibition capillary number. The imbibition capillary number was altered by changing the imbibition velocity (or flowrate). While Kimbrel et al. (2015), examined both the isolated and combined parameters of the capillary number's influence on residual trapping, primarily focusing on the imbibition flowrate through mildly consolidated sintered glass bead packs. The study determined that imbibition flowrate had no significant effect on residual trapping.

Additionally, Blunt and Scher (1995) used a network model to show that increases in flowrate decreases the residual nonwetting phase saturation. Cao et al. (2015) conducted experiments in 2-D micromodels and found increasing $scCO_2$ injection rate (drainage rate) resulted in a larger amount of displaced brine (or more $scCO_2$ in the system post-drainage).

Further, the oil-recovery study by Chatzis and Morrow (1984) used capillary number relationships to show the greater difficulty that exists when removing disconnected oil blobs compared to well-connected (or continuous) oil. In this work capillary number is similarly referred to as the ratio of viscous and capillary forces, however some definitions do incorporate media permeability.

The independent and combined effects of drainage and imbibition flowrate on residual nonwetting phase capillary trapping, has not, to our knowledge, been investigated.

3.4 Topology

Topology (or connectedness) is a metric that has recently been introduced for use in multiphase flow through porous media studies. Studies have looked at the influence of media topology or pore structures on residual nonwetting phase trapping. Tanino and Blunt (2012), performed studies in limestone and sandstone utilizing the pore coordination number and pore body-throat aspect ratio. The pore coordination number represents the number of pore throats connected to a certain pore body. This study found residual nonwetting phase trapping to decrease with smaller pore aspect ratios and increasing coordination number, which represent unfavorable conditions for snap-off. Al-Raoush and Willson (2005), performed experiments in glass bead packs and found nonwetting phase trapping to occur in pore-bodies with large pore body-throat aspect ratio and coordination number. Andersson et al. (2018), introduced a new method for describing the pore body-throat aspect ratio, the ‘Morphological Aspect Ratio’ or MAR. MAR utilizes the Euler number to describe pore-space connectedness. This study, performed on Bentheimer sandstone and various glass bead cores, found the residual nonwetting phase trapping to scale with MAR, a

high connectivity of the pore space loosely correlates to more residual nonwetting phase trapping (S_r).

Additional studies analyze topology of the nonwetting phase fluid to understand residual nonwetting phase trapping. Herring et al. (2013), utilized a normalized Euler number of the nonwetting phase (the Euler number of a particular sample by the maximum Euler number of the nonwetting phase, 100% saturation) to compare nonwetting phase fluid topology of multiple pore geometries (Bentheimer sandstone, glass bead columns of different packings, and crushed tuff). This study concluded that nonwetting phase trapping in Bentheimer sandstone is dependent on post-drainage nonwetting phase connectivity and the imbibition capillary number.

This work utilizes the Euler number of the nonwetting phase to analyze the influence of post-drainage connectivity of the nonwetting phase on residual nonwetting phase trapping (S_r).

3.5 Experimental design

Previous laboratory scCO_2 sequestration studies have involved 2-D systems and pore-scale 3-D experiments that require x-ray tomography imaging in order to visualize fluid flow. While 2-D systems are fundamental to the better understanding of general fluid behavior, CO_2 sequestration occurs at reservoir scale and effort to characterize 3-D fluid flow is essential. To date 3-D experiments have been conducted and fluids visualized at high-resolution, usually around 5-10µm (e.g. Wildenschild and Sheppard 2013) and experimental set-up and image processing for this type of work is time consuming. Therefore, a 3-D experimental design that reduces the complexity of experimental set-up, imaging, and data analysis is desired.

Chapter 4: Materials and Methods

4.1 Porous media masks

Porous media masks were 3-D printed with polylactide (PLA) in order to resemble 700µm bead packs in uniform cubic, non-uniform cubic, and non-uniform rhombohedral arrangements (Figure 9 and 10). 700µm diameter beads are comparable to sandstone grain diameters. In this work, non-uniform refer to the presence of high porosity zones in that specific bead pack. The non-uniform cubic bead pack has a significantly greater number of high porosity zones than the non-uniform rhombohedral bead pack. All masks were printed to identical sizes of 44.8mmX44.8mmX2.8mm, in order to securely fit in the flow cell. All masks are four rows of beads thick (2.8mm), to allow for 3-D flow. The system will be referred to as a pseudo-3-D system due to the smaller fraction of pore space in the third dimension (2.8mm compared to 44.8x44.8mm).

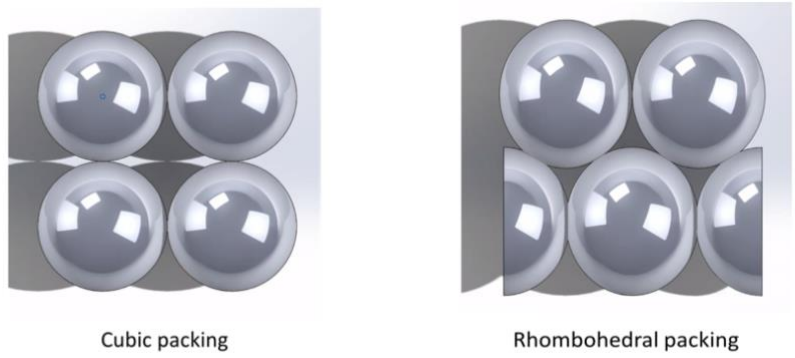

Figure 9: Bead pack arrangements. All beads are 700µm in diameter.

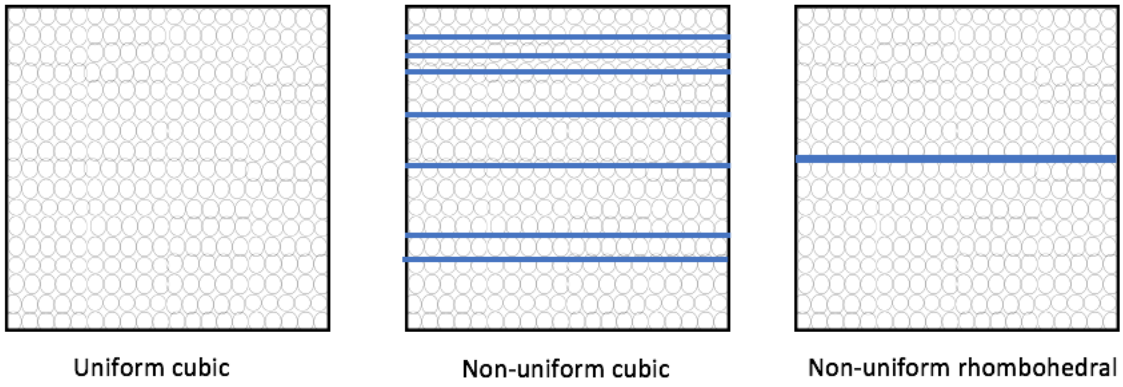

Figure 10: Representation of different bead pack arrangements. General placement and quantity of high porosity zones is presented (blue lines).

Porosity is calculated by measuring the mass of the bead pack (grams) and obtaining the density of PLA (g/cm^3). Volume of the PLA can then be calculated:

$$\text{Volume of material} = \frac{\text{Mass of material}}{\text{Density of material}}$$

Equation 10

The overall volume of the bead pack is then calculated by the dimensions 44.8mmX44.8mmX2.8mm. Void volume can then be calculated:

$$\text{Void volume} = \text{Volume of bead pack} - \text{Volume of material}$$

Equation 11

The porosity of the bead pack is then calculated:

$$\text{Porosity (\%)} = \frac{\text{Void volume}}{\text{Volume of bead pack}} \times 100$$

Equation 12

Table 1: Porous media properties		
Geometry	**Single Bead Diameter (μm)**	**Measured Porosity (%)**
Uniform cubic	700	36.9
Non-uniform cubic	700	37.4
Non-uniform rhombohedral	700	33.7

4.2 Fluid Pairs

All experiments were conducted using proxy-fluids in order to mimic the $scCO_2$-brine-sandstone, high pressure and temperature, $scCO_2$ sequestration scenario. Soltrol® 220 (Soltrol) (wetting phase) and dyed water (nonwetting) were used throughout all experiments at ambient temperature and pressure.

4.2.1 Wettability

Wettability alteration of the polylactide (PLA) bead packs was tested by submerging two flat pieces of PLA in Soltrol, one for 4 hours and one for 5 days. Contact angles were then measured with a goniometer on all previously submerged PLA pieces and an untreated (not previously submerged) piece of PLA. There existed no systematic difference in contact angles measured in any of the submerged pieces of PLA in comparison to the untreated piece. Contact angles ranged from 0-16° on all PLA pieces (submerged and untreated) depending on the area of the PLA piece the measurement was taken. The 3-D printed PLA pieces had some imperfections in the surfaces which influenced contact angle measurements and are responsible for the range measured (0-16°) on all pieces. Contact angles between 0° and 65-70° between the wetting fluid and the media is referred to as a wetting system (Anderson, 1987). We therefore conclude, that wettability alterations, within the experimental timeframe, are not a concern for this set-up.

Table 2: Fluid properties				
Fluid Pair	**Wetting Phase Viscosity (cP)**	**Nonwetting Phase Viscosity (cP)**	**Interfacial Tension (dynes/cm)**	**Wetting Phase Wettability**
Soltrol-water	4.82	1.13	25	0 - 16°
Brine-scCO$_2$	1.13	0.025-0.15[a]	20-50[b]	-

a.) Bachu, 2003
b.) Bachu and Bennion, 2008

4.3 Experimental Set-Up

Experiments were conducted at ambient temperature and pressure. The 3-D printed porous media masks were inserted into the flow cell base and enclosed by first the transparent cover and then the frame. The flow cell base has an etched compartment (44.8x44.8x2.8mm) so the bead packs fit securely and are sealed by overlaying the transparent cover. The flow cell base is polycarbonate and the transparent cover is acrylic, both of which are wetted by Soltrol. All layers were connected to each other and secured with screws (Figure 11 and 12).

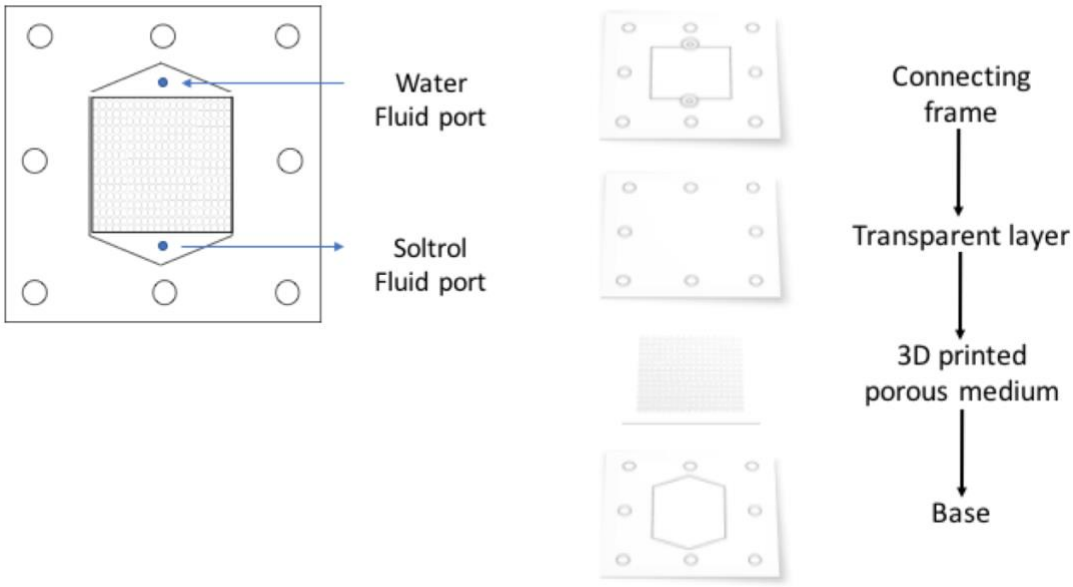

Figure 11: Schematic of flow cell design.

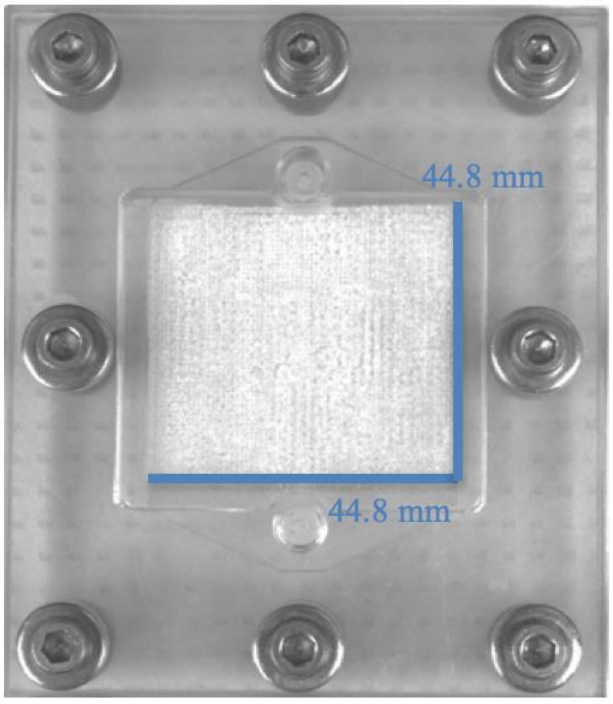

Figure 12: Flow cell with three-dimensional mask secured in center

Fluid was introduced and controlled through ports on either side (top and bottom) of the medium with 1/16-inch inner diameter Tygon® tubing. A Harvard PhD Ultra Syringe pump precisely controlled the imbibition (injection of Soltrol) and drainage (withdrawal of water) processes, by altering the direction of the pump. Pressure was monitored and recorded using a Validyne differential pressure transducer (maximum differential pressure of 144cm) connected to the system.

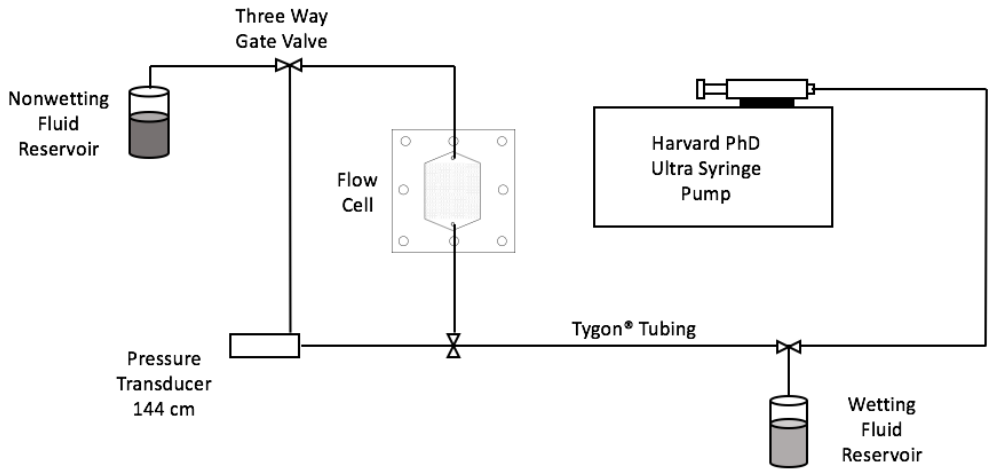

Figure 13: Experimental Set-up. The flow cell is connected to 1/16-inch inner diameter Tygon® tubing, a Harvard PhD Ultra Syringe pump, and Validyne differential pressure transducer (144 cmH2O).

4.4 Experimental Procedure

A clean, dry bead pack was inserted in the flow cell and connected to the remainder of the system (tubing, transducer, and pump) for each experiment. The transducer was calibrated at the beginning of each experiment. The flow cell was then secured horizontally (to remove the impact of gravity and isolate the effect of flowrate in the system) five centimeters above the lab bench, to ensure no shadows would appear in the images from the base of the system.

A Canon EOS T5i and tripod were then secured above the flow cell for imaging. The flow cell was imaged when the system was saturated with Soltrol (after initial imbibition). This provided an initial image of the system, documenting air bubbles introduced through the initial saturation event.

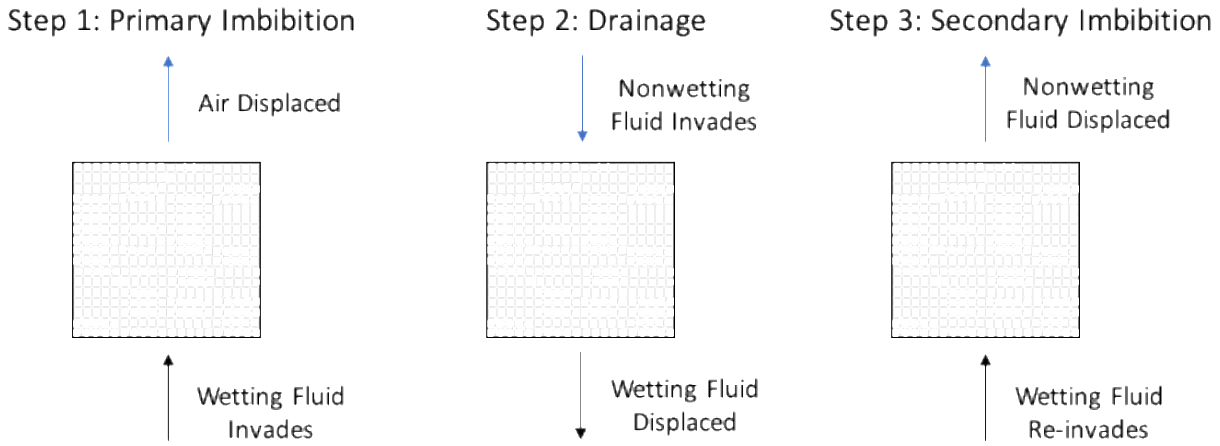

Figure 14: Primary imbibition, drainage, and secondary imbibition. Images were taken after each step.

After the initial image of a fully Soltrol-saturated system, the next step involved draining the system (in which water the nonwetting fluid displaced Soltrol the wetting fluid) at either 0.5 or 42 ml/hr. These rates placed the system in either a stable region dominated by capillary forces (0.5 ml/hr) or in an area closer to the viscous dominated region (42 ml/hr) on the Lenormand diagram (Figure 7). The system was imaged throughout the drainage cycle. When the first drop of nonwetting fluid was drained from the bead pack, the drainage process was stopped. After an equilibration period of 15 minutes, the system was imaged again.

Once the post-drainage image was complete, the wetting phase (Soltrol) was re-imbibed into the system in the third step (Figure 14) at either 0.5 or 42 ml/hr. These rates again placed the system in either a region dominated by capillary forces or viscous forces on the Lenormand diagram. The

system was imaged throughout the imbibition cycle. Imbibition continued until Soltrol entered the top trough of the flow cell to ensure remaining nonwetting fluid in the system was trapped. After an equilibration period of 15 minutes, the system was imaged again.

Experiments were conducted, on the uniform cubic arrangement, by altering both the drainage and imbibition flowrate (Table 3), in order to analyze the independent and combined influences of flowrate, during each phase, on trapping.

Table 3: Experimental properties for uniform cubic bead pack

Experiments	**Drainage Flowrate (ml/hr)**	**Drainage Capillary Number**	**Drainage Mobility Ratio**	**Imbibition Flowrate (ml/hr)**	**Imbibition Capillary Number**	**Imbibition Mobility Ratio**
Fast, fast	42	1.13×10^{-5}	0.23	42	4.82×10^{-5}	4.27
Slow, slow	0.5	1.25×10^{-7}	0.23	0.5	5.35×10^{-7}	4.27
Fast, slow	42	1.13×10^{-5}	0.23	0.5	5.35×10^{-7}	4.27
Slow, fast	0.5	1.25×10^{-7}	0.23	42	4.82×10^{-5}	4.27

Experiments were then conducted on non-uniform cubic and non-uniform rhombohedral arrangements (Table 4), in order to analyze and compare trapping trends to those observed in the uniform cubic experiments.

Table 4: Experimental properties for non-uniform cubic and rhombohedral bead packs

Experiments	**Drainage Flowrate (ml/hr)**	**Drainage Capillary Number**	**Drainage Mobility Ratio**	**Imbibition Flowrate (ml/hr)**	**Imbibition Capillary Number**	**Imbibition Mobility Ratio**
Fast, fast	42	1.13×10^{-5}	0.23	42	4.82×10^{-5}	4.27
Slow, slow	0.5	1.25×10^{-7}	0.23	0.5	5.35×10^{-7}	4.27

4.5 Image Acquisition and Processing

All images were captured using a Canon EOS Rebel T5i. Images collected throughout experiments were saved as raw image files. Image processing was performed with ImageJ software. The goal of image processing is to isolate and quantify the nonwetting phase.

4.5.1 Segmentation

The first image processing step is to register (or align) all collected images (post-primary imbibition, post-drainage, and post-secondary imbibition) and remove air bubbles. Air bubbles should be removed from images, as to not be considered in future calculations. This is accomplished by calculating the difference between images, the absolute value of post-drainage minus post-primary imbibition and absolute value post-secondary imbibition minus post-primary imbibition (Figure 15 a,b,c).

A minimum filter (4 pixels) is then applied to all images to remove small pixel values associated with noise and remaining air bubbles (Figure 15d, 16a and 16b). Images are then converted to an 8-bit image file, in order to segment the image. Segmentation allows for distinction of phases (nonwetting from the medium and wetting phase). Segmentation was accomplished with the Otsu method (Otsu, 1979). Segmentation results in a binary (black and white) image (Figure 15e) with corresponding intensity values of either 0 or 255 (Figure 16c). White references the nonwetting phase and black references the porous medium and wetting phase.

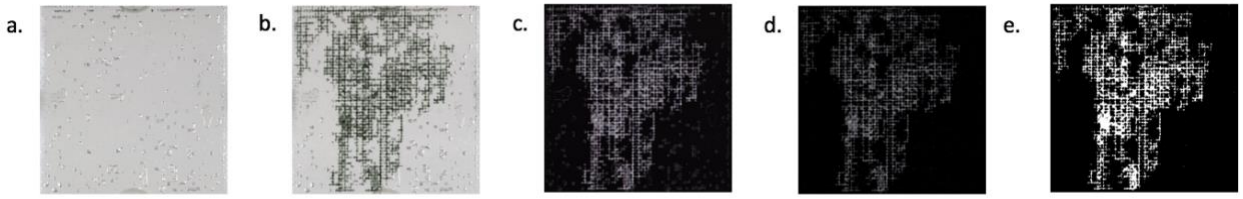

Figure 15: Image processing of post-drainage image (Slow, slow experiment in uniform cubic bead pack). a.) Original image captured post-primary imbibition, after system was allowed to equilibrate. b.) Original image captured post-drainage, after system was allowed to equilibrate. c.) Difference in images a and b. d.) Minimum (4-pixel) filter applied. e.) Otsu automatic segmentation results.

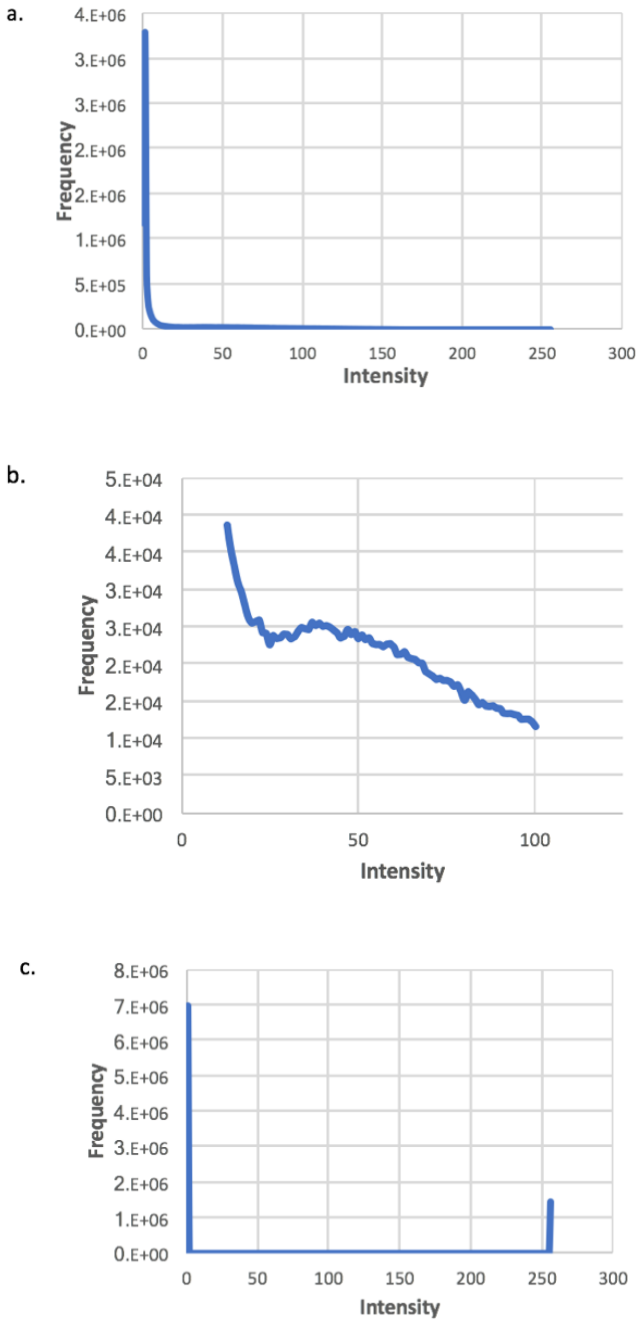

Figure 16: Resulting histograms of processed images. a.) Histogram of filtered image before automatic segmentation. b.) Zoomed-in on previous histogram (a), shows dip automatic thresholding locates for segmentation. c.) Resulting histogram after Otsu method segmentation. Intensity values after segmentation are either 0 or 255, due to the resulting binary image. Intensity value of 0 corresponds to the medium and wetting phase in the image and an intensity value of 255 corresponds to the nonwetting phase in the image.

4.5.2 Quantifying the nonwetting phase

The total number of pixels in an image is determined by the image dimensions. For example, 2900 pixels by 2900 pixels (Figure 17). The area of the image ($pixels^2$) was then calculated (8,410,000 $pixel^2$). The porosity of the corresponding porous medium is calculated (Equation 10, 11, and 12) and multiplied by the area of the image, to determine the fraction of pixels that represent area where fluid could be, or void spaces. This calculated number of pixels of void space, was then used to determine the fraction of void spaces occupied by the nonwetting phase. The number of pixels that had a 255-intensity value, which corresponds to nonwetting phase or white (Figure 16c and 17), were divided by this new pixel count and determined the fraction of void spaces occupied by nonwetting phase.

The pseudo-3D nature of the bead pack allows 3-D fluid flow, which allows the nonwetting phase fluid to reside in various layers (one to multiple layers). Because we are representing the pseudo-3D bead packs with a 2-D image, the assumption is made that all the nonwetting phase in an image is contained within in a single pore layer. While this assumption still allows for fluid flow trends to be quantified between different flowrates, the overall percentages of nonwetting phase presented is higher than is actually present.

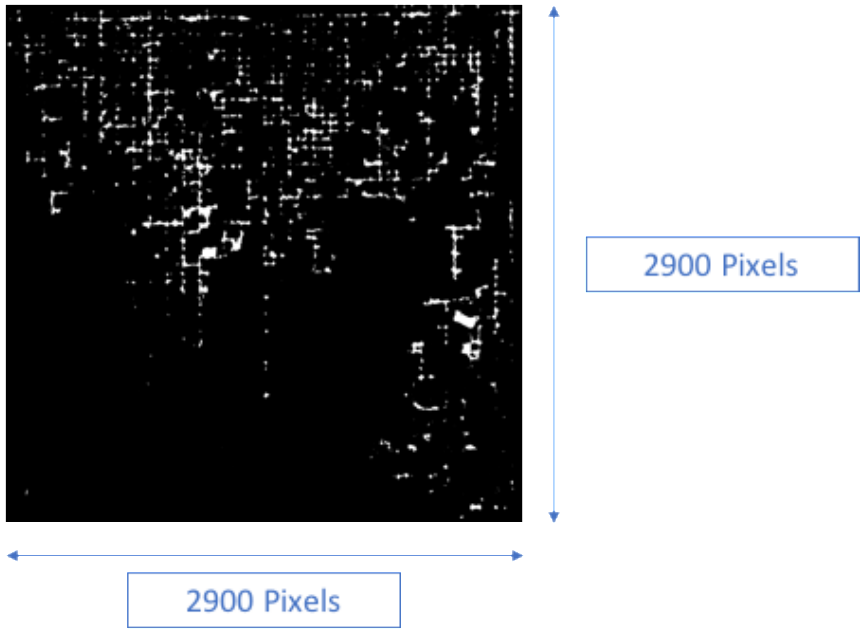

Figure 17: Total number of pixels in image

Chapter 5: Results and Discussions

The effects of drainage and imbibition flowrate on the trapped amount of nonwetting phase are presented in this chapter. Trapping efficiencies are analyzed through uniform cubic, non-uniform cubic, and non-uniform rhombohedral bead packs.

5.1 Uniform cubic arrangement

Results presented in this section are for experiments performed on uniform cubic bead packs.

5.1.1 Dominating Forces

The Lenormand phase diagram (Figure 18) is used to predict the dominating forces that influence fluid flow during drainage. The Lenormand diagram is composed of the log of capillary number and mobility ratio (Equation 5 and 7). Therefore, provided a single fluid pair (in this work, Soltrol and water) velocity is the only parameter that can be altered within an experiment to change the capillary number and ultimately the placement of an experiment on the Lenormand diagram. The region boundaries on the Lenormand diagram are system dependent (Lenormand et al., 1988; Zhang et al., 2011). The experiments presented in this work were conducted at flowrates of 0.5 ml/hr and 42 ml/hr, placing experiments in distinct regions of the diagram (Figure 18) and resulting in unique fluid flow regimes between flowrates (Figure 19). Slow experimental flowrate (0.5 ml/hr) results in a more capillary dominated flow regime (Figure 18 and 19), while, fast experimental flowrate (42ml/hr) results in a more viscous dominated flow regime (Figure 18 and 19). Visual distinction of capillary and viscous dominated flow regimes is readily apparent in the uniform cubic arrangement due to the simple nature of a cubic geometric arrangement (Figure 9).

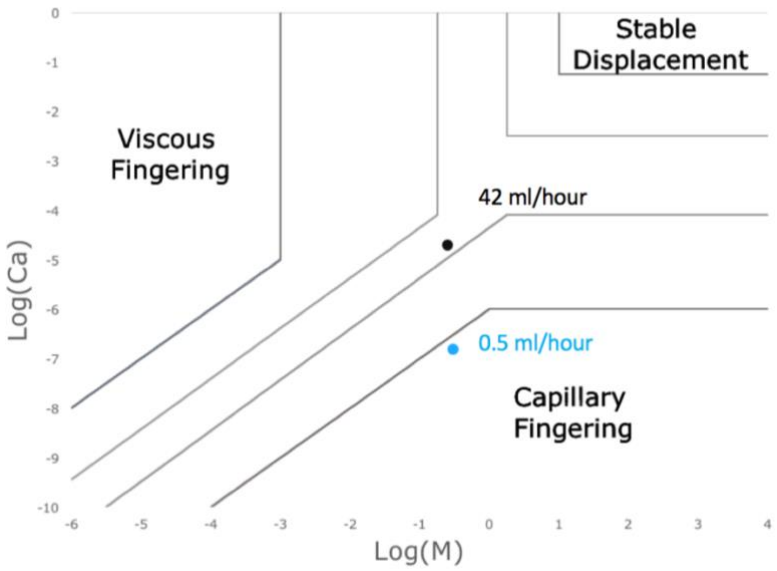

Figure 18: Lenormand phase diagram with presented experiments.

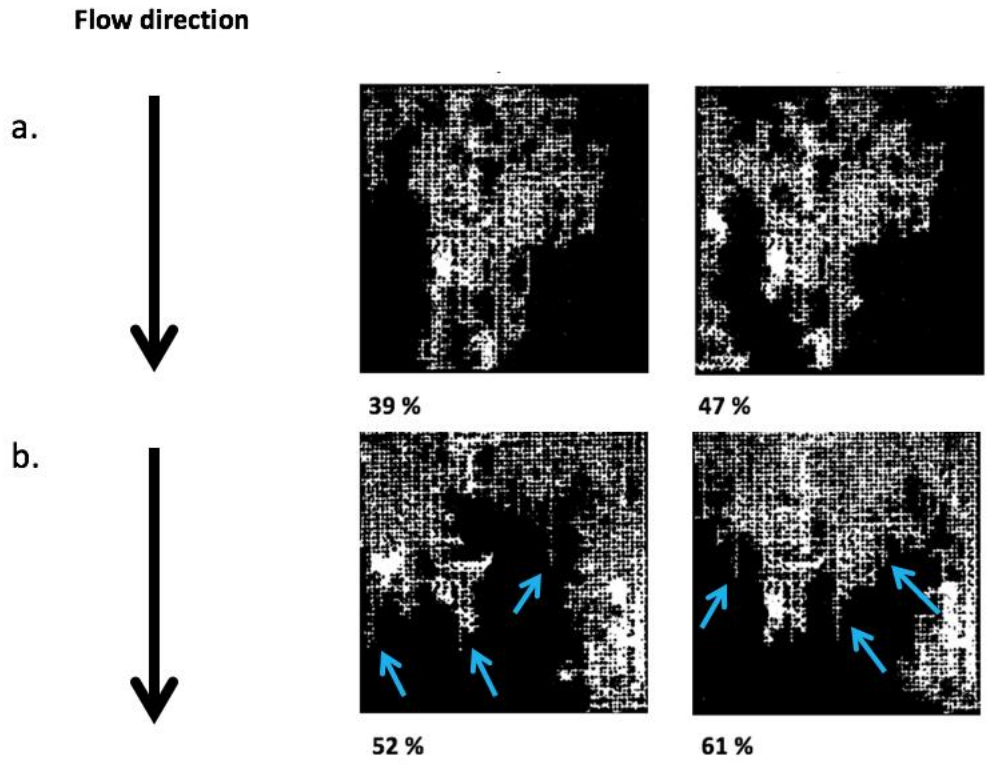

Figure 19: a.) Result of two slow (0.5ml/hr) drainages on uniform cubic bead packs. Capillary force dominated flow pattern is present. b.) Result of two fast (42ml/hr) drainages on uniform cubic bead packs. Viscous force dominated flow pattern is present illustrating isolated fingered flow (blue arrows).

5.1.2 Flowrate

Experiments were conducted by altering both the drainage and imbibition flowrate (Table 3), in order to analyze the independent and combined influences of flowrate, during each flow phase, on trapping. Flowrates during both the drainage and imbibition phase, are observed to have an influence on the overall trapped nonwetting phase (S_r). Flow regimes and corresponding dominating forces also appear to influence fluid flow behavior and overall trapping (Figure 20).

Fast drainages (42ml/hr) result in a larger amount of nonwetting phase post-drainage (S_I) compared to slow drainages (0.5ml/hr) (Figure 20 and Table 5). However, when analyzed with subsequent imbibition phases (S_r), slow drainages (0.5ml/hr) are more efficient than fast drainages (42ml/hr). Slow drainages, regardless if paired with a slow or fast imbibition phase, result in greater trapping efficiency of the nonwetting phase. In these experiments, a slow flowrate (0.5ml/hr) results in a more capillary dominated flow. Therefore, a more capillary dominated drainage, regardless if followed by a viscous or capillary dominated imbibition, results in the most efficient trapping of the nonwetting phase (S_r/S_I). All quantified experimental images, for drainage and imbibition, are presented in Figure 21.

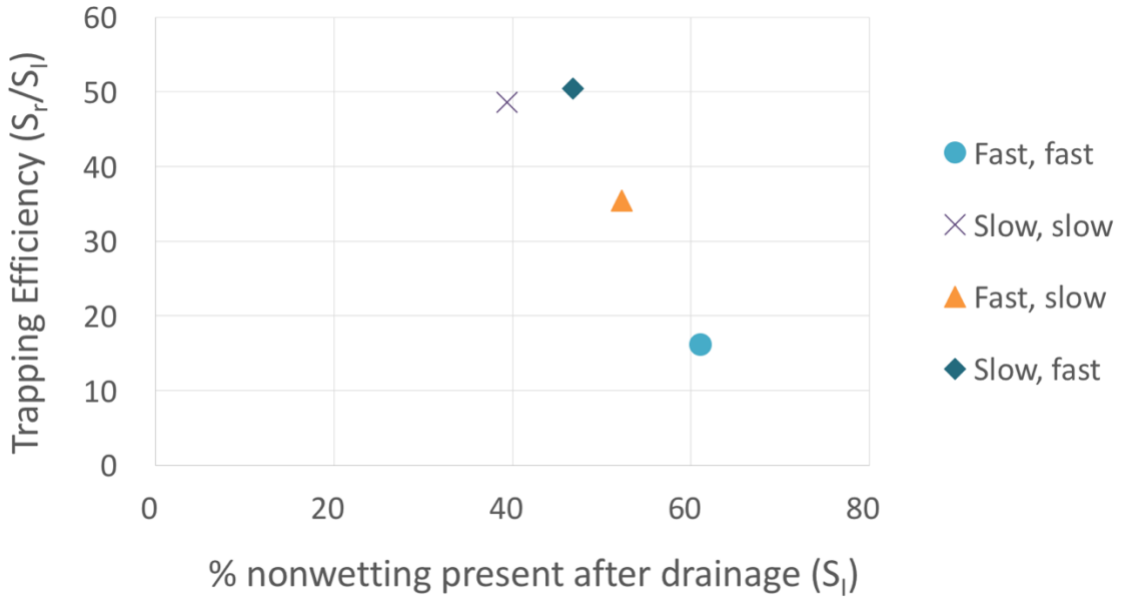

Figure 20: Trapping efficiency (S_r/S_I) for uniform cubic experiments. Fast is 42 ml/hr and slow is 0.5 ml/hr.

Table 5: Experimental flowrates and percent nonwetting phase trapped after drainage and imbibition

Experiment	Drainage Rate (ml/hr)	% Trapped after drainage (S_I)	Imbibition Rate (ml/hr)	% Trapped after imbibition (S_r)	Trapping Efficiency (S_r/S_I)
Fast, fast	42	61	42	10	16
Slow, slow	0.5	39	0.5	19	49
Fast, slow	42	52	0.5	19	37
Slow, fast	0.5	47	42	24	51

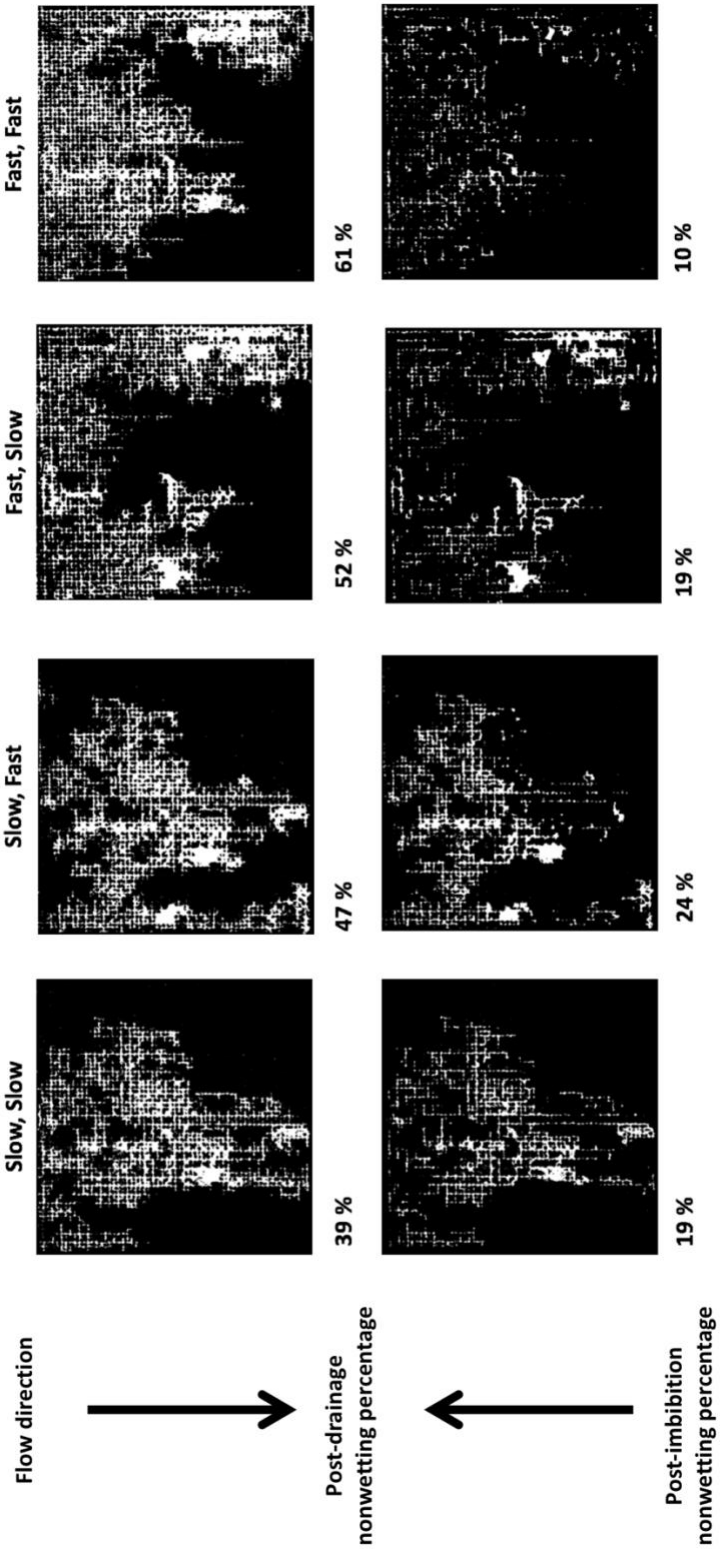

Figure 21: Quantified experimental results for each uniform cubic experiment.

5.1.3 Topology

An object with a higher connectivity (or more redundant connections) has a more negative Euler number (Figure 6). Therefore, experiments with more negative initial Euler number have higher connectivity of the nonwetting phase post-drainage (Figure 22). In this work, fast drainages (42ml/hr) result in more negative initial Euler numbers, while, slow drainages (0.5ml/hr) result in more positive initial Euler numbers (Figure 22). This suggests that fast drainage results in higher connectivity of the nonwetting phase compared to slow drainage.

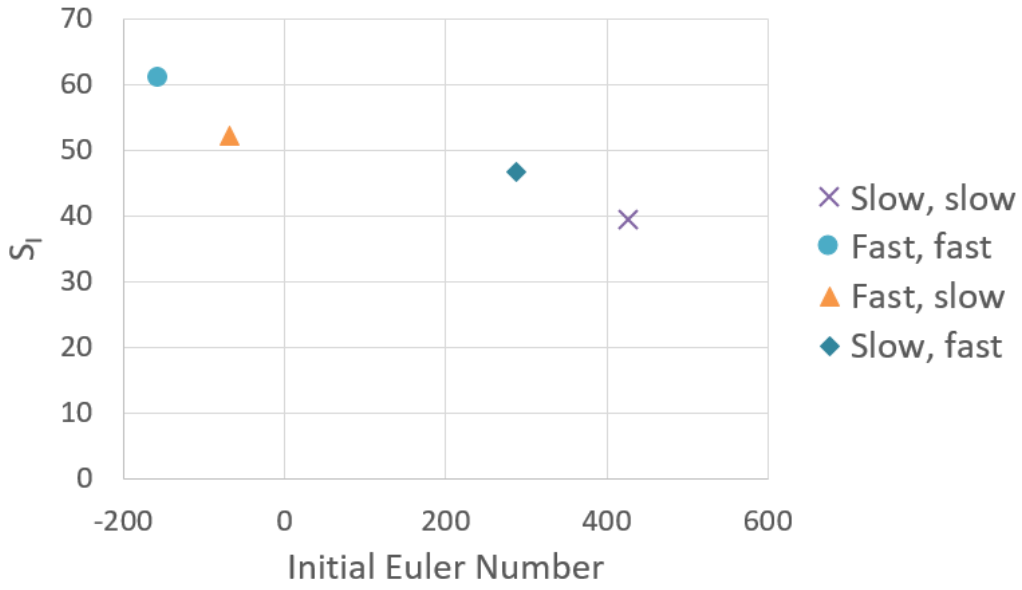

Figure 22: Initial Euler number (connectivity metric) and nonwetting phase saturation of all uniform cubic arrangement experiments after drainage.

Fast drainages (42 ml/hr) resulted in less efficient trapping of the nonwetting phase compared to slow drainage (0.5 ml/hr) (Figure 20). This, paired with the greater connectedness of the nonwetting phase after fast drainage (Figure 22), suggests that high connectivity after drainage is nonconductive to trapping efficiency (Figure 23 and Table 6).

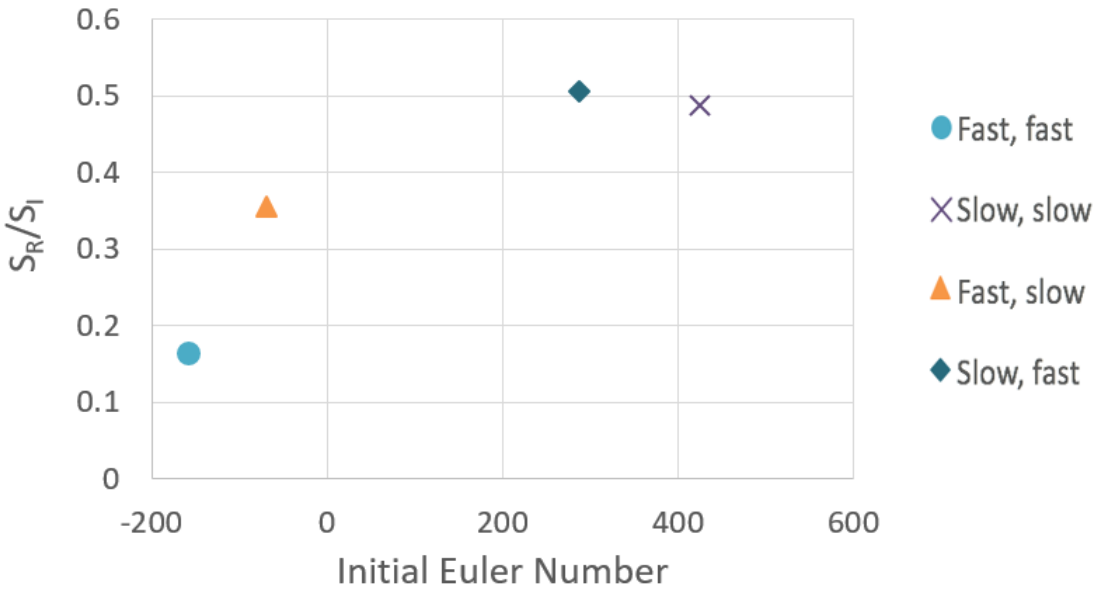

Figure 23:Trapping efficiency as a function of initial Euler number in a uniform cubic arrangement.

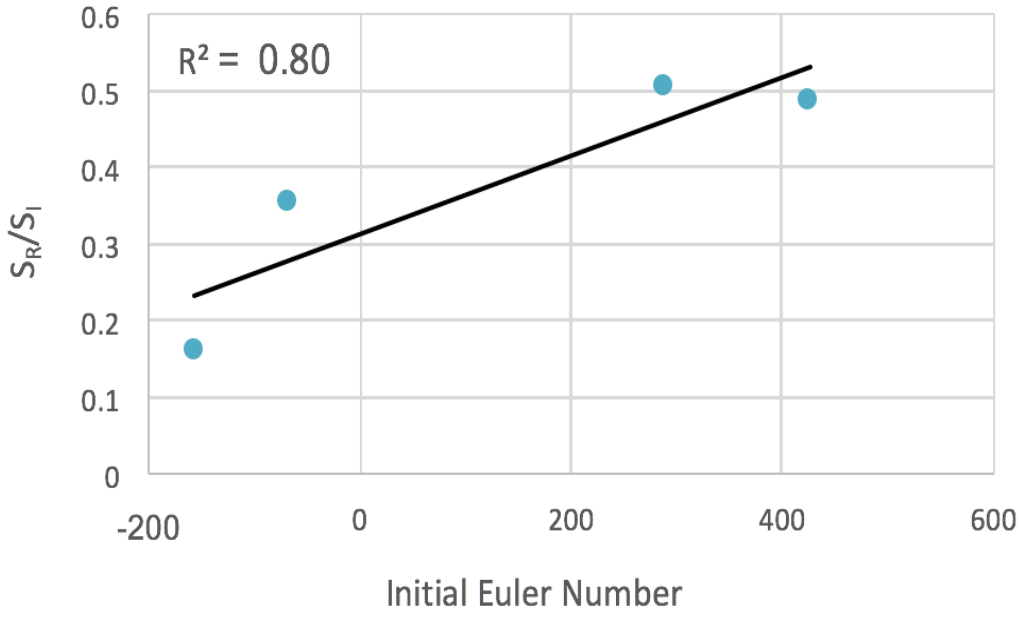

Figure 24: Initial Euler numbers influence on trapping efficiency on uniform cubic arrangement with linear trend line.

Table 6: Connectivity values after drainage for a uniform cubic arrangement.		
Experiments	**Initial Euler Number**	**% nonwetting phase trapped (S_r/S_I)**
Slow, slow		
Slow Drainage	426	49
Fast, fast		
Fast Drainage	-157	16
Fast, slow		
Fast Drainage	-68	37
Slow, fast		
Slow Drainage	288	51

5.1.4 Air bubbles

Despite precautions to eliminate the trapping of air bubbles during primary imbibition, a small amount of air was present at the beginning of each experiment. Further, each experiment began with a dissimilar amount of air bubbles after primary imbibition and before drainage. We believe this inconsistency within the start of experiments contributes to the difference in nonwetting phase present after drainage for multiple experiments with the same drainage flowrate (Figure 25 and 26). Experiments that had more bubbles after primary imbibition and before primary drainage had less nonwetting phase after the drainage cycle. We believe this is due to the air bubbles occupying more pore spaces, leaving less pores for the nonwetting phase to advance through. Despite the presence of air bubbles influencing the amount of nonwetting phase present after primary drainage for experiments conducted at the same drainage flowrate, resulting flow patterns were still similar for these experiments.

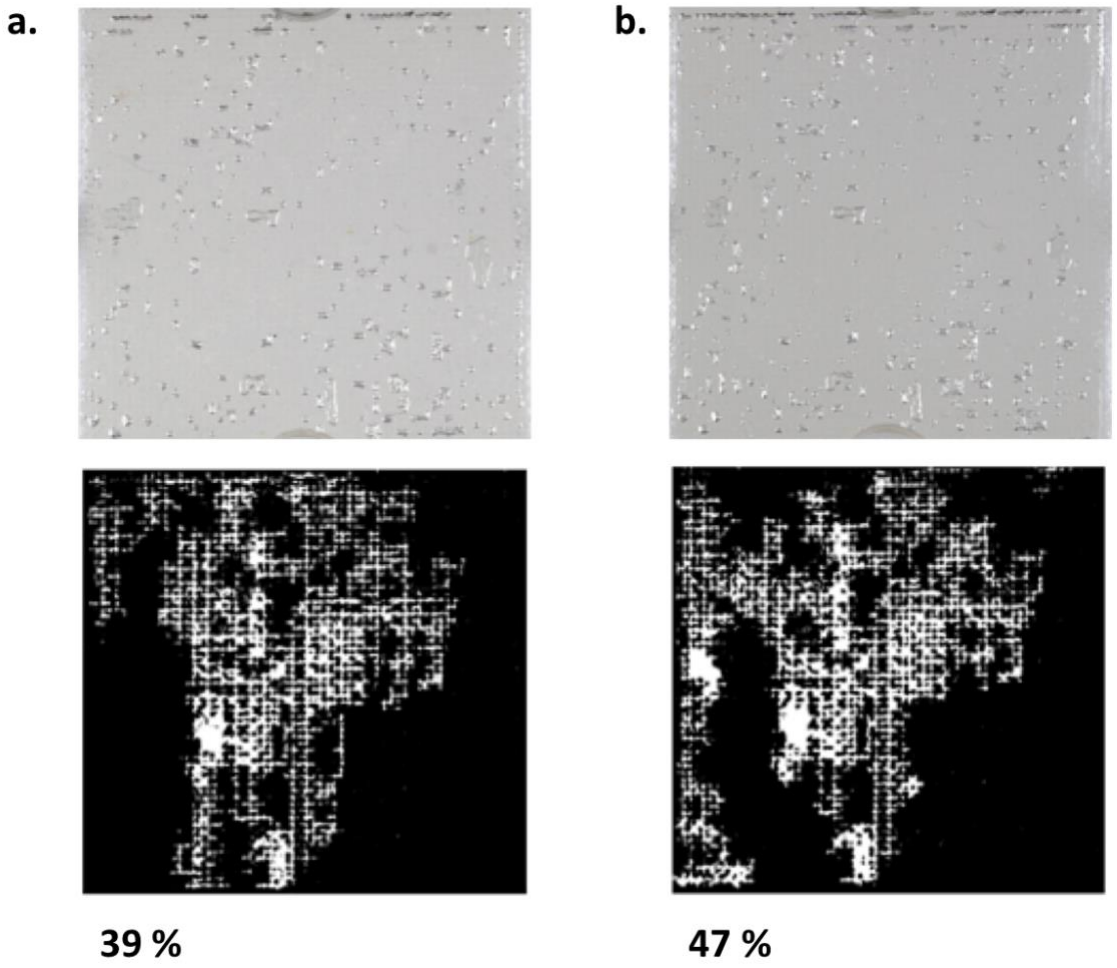

Figure 25: Dissimilar amount of air bubbles present before both 0.5ml/hr drainages contributes to the amount of nonwetting phase present after the drainage event. Image series a has more initial bubbles than image series b, resulting in less nonwetting phase after drainage.

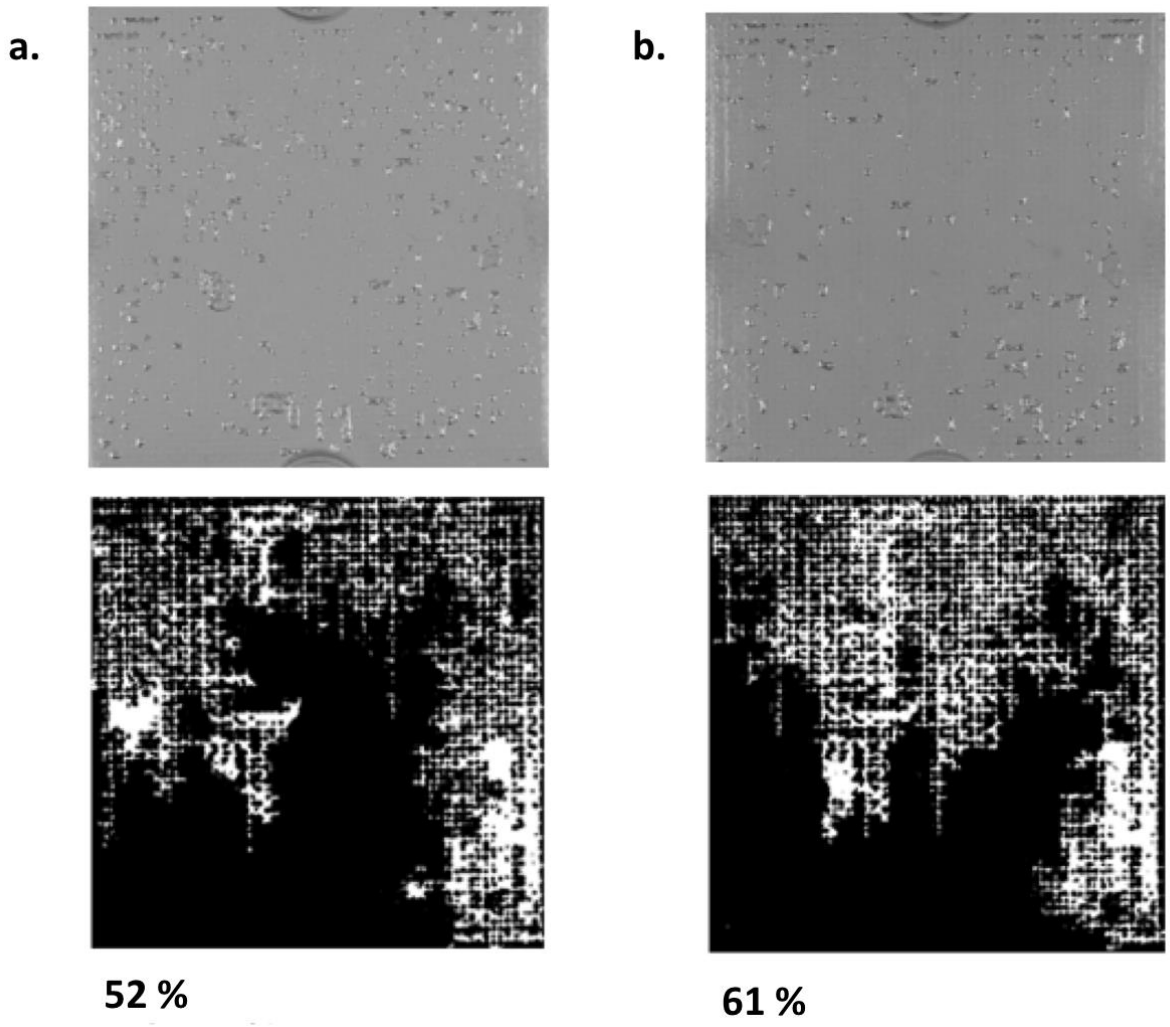

Figure 26: Dissimilar amount of air bubbles present before both 42ml/hr drainages contributes to the amount of nonwetting phase present after the drainage event. Image series a has more initial bubbles than image series b, resulting in less nonwetting phase after drainage.

5.2 Non-uniform cubic arrangement

Experiments on the non-uniform cubic packing arrangement were conducted at fast (42ml/hr) and slow (0.5ml/hr) flowrates, similar to the flowrates performed on the uniform cubic arrangement, in order to analyze and compare nonwetting phase trapping between the bead packs. All quantified experimental images, for drainage and imbibition, are presented in Figure 27.

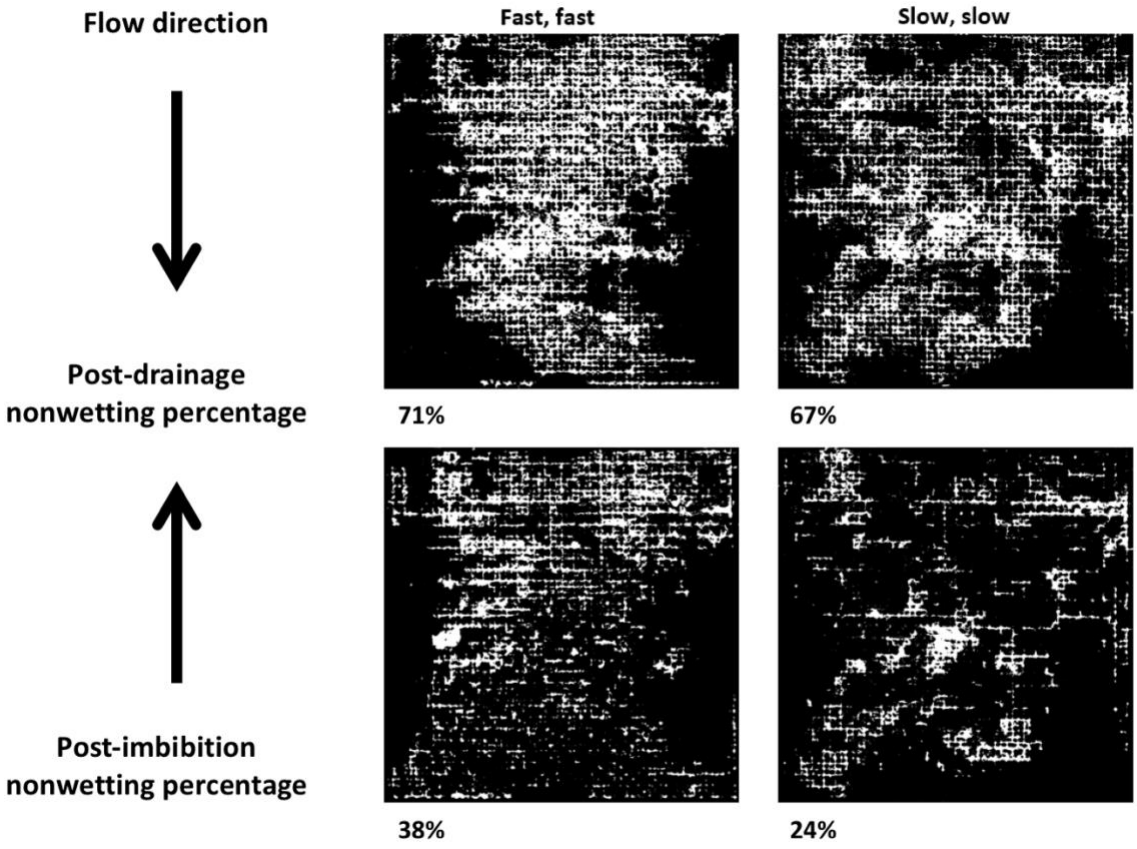

Figure 27: Quantified experimental results for each non-uniform cubic experiment.

In regard to dominating forces in the non-uniform cubic arrangement, drainage flowrates (42 ml/hr and 0.5 ml/hr) and fluid properties (Table 2) were the same as those in the uniform cubic experiments, indicating that flow regimes and dominating forces remain predictable via the

Lenormand diagram (Figure 18). However, observations of distinct viscous fingering post-drainage in the non-uniform cubic arrangement are less visible compared to those observed in the uniform cubic arrangement (Figure 27). This is attributed to the high-porosity zones essentially restricting long viscous fingered flow in the non-uniform cubic bead pack.

Fast drainages (42ml/hr) still result in a larger amount of nonwetting phase post-drainage (S_I) compared to slow drainages (0.5ml/hr) (Figure 28 and Table 7). However, when analyzed with subsequent imbibition phases (S_r), slow drainages (0.5ml/hr) are *not* more efficient than fast drainages (42 ml/hr), which was observed in uniform cubic experiments. This observed alteration in the nonwetting phase trapping efficiency trend is attributed to the high-porosity zones present in the non-uniform cubic bead pack. As the initial Euler numbers observed in the non-uniform cubic arrangement follow those observed in the uniform cubic arrangement, more disconnect of the nonwetting phase is present after slow drainages compared to fast drainages (Figure 29 and Table 8). This lends to the understanding that the same drainage flow regimes occur in the non-uniform cubic arrangements, as do in the uniform cubic bead packs. However, during imbibition, the nonwetting phase previously brought into the system during drainage (S_I) gets trapped behind the high-porosity zones. So, despite the disconnect of the nonwetting phase post-slow drainage, that was previously shown to be conducive to trapping efficiency in the uniform cubic bead pack, the system with the most nonwetting phase present after drainage (S_I) will be more efficient in a highly non-uniform system, as there is more nonwetting phase present to be trapped behind the high-porosity zones during imbibition.

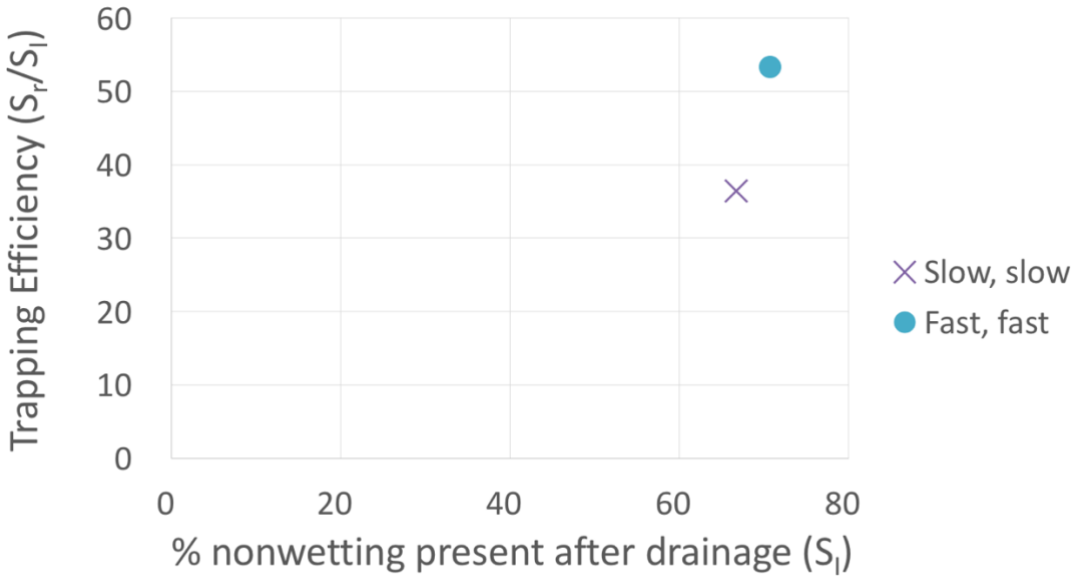

Figure 28: Trapping efficiency (S_r/S_I) for non-uniform cubic experiments.

Table 7: Experimental flowrates and percent nonwetting phase trapped after drainage and imbibition for non-uniform cubic arrangement					
Experiment	**Drainage Rate (ml/hr)**	**% Trapped after drainage (S_I)**	**Imbibition Rate (ml/hr)**	**% Trapped after imbibition (S_r)**	**Trapping Efficiency (S_r/S_I)**
Fast, fast	**42**	**71**	**42**	**38**	**54**
Slow, slow	**0.5**	**67**	**0.5**	**24**	**36**

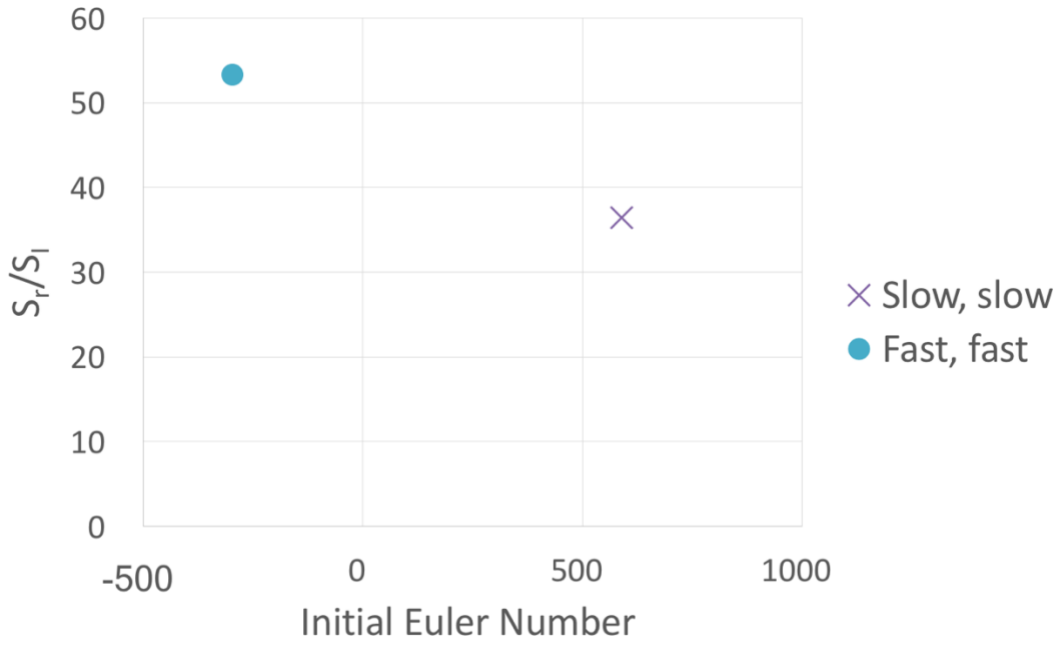

Figure 29: Trapping efficiency as a function of initial Euler number in a non-uniform cubic arrangement.

Table 8: Connectivity values after drainage for a non-uniform cubic arrangement.

Experiments	**Initial Euler Number**	**% nonwetting phase trapped (S_r/S_I)**
Slow, slow		
Slow Drainage	590	36
Fast, fast		
Fast Drainage	-298	54

5.3 Non-uniform rhombohedral arrangement

Experiments on the non-uniform rhombohedral arrangement were conducted at fast (42ml/hr) and slow (0.5ml/hr) flowrates, similar to the flowrates performed on both the uniform cubic and non-uniform cubic arrangements. This again allowed the trend of nonwetting phase trapping in non-uniform rhombohedral bead packs to be analyzed and compared to those observed in the uniform and non-uniform cubic bead packs. All quantified experimental images, for drainage and imbibition, are presented in Figure 30.

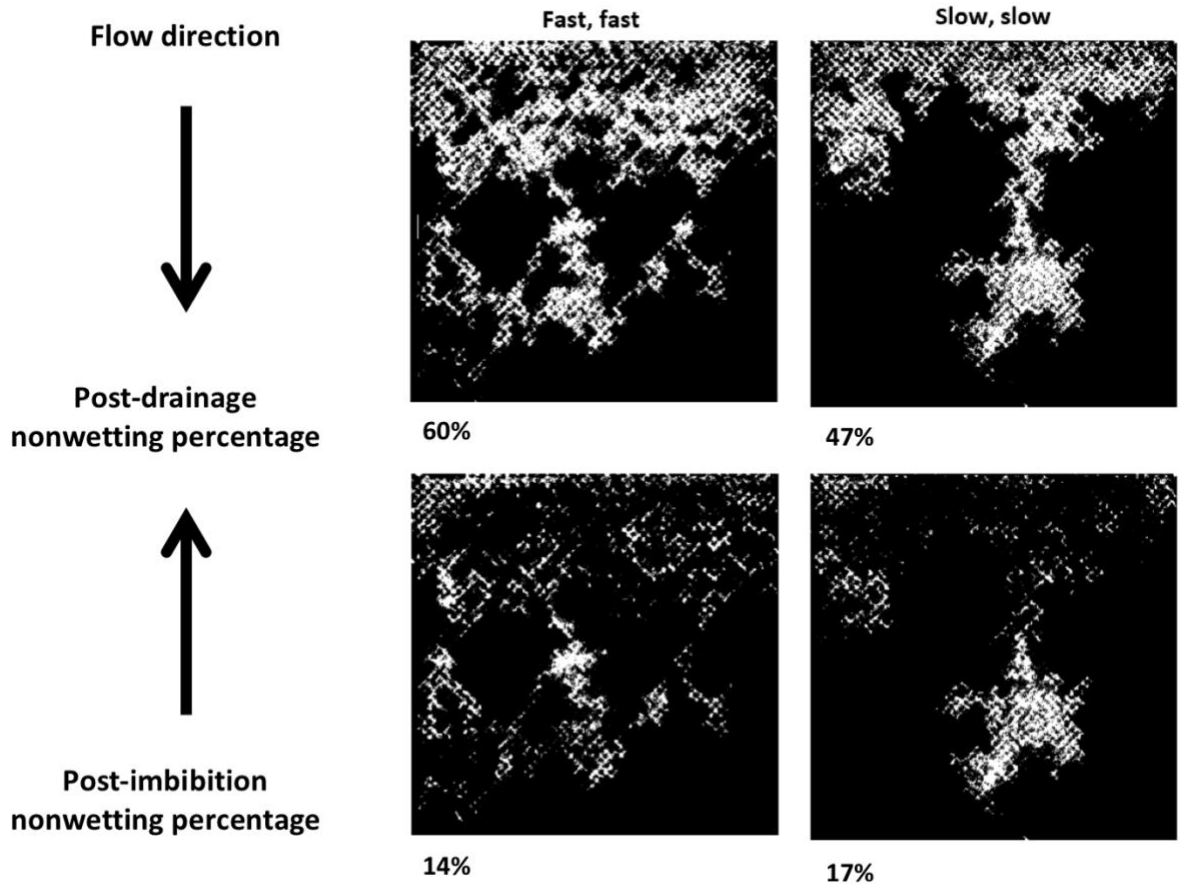

Figure 30: Quantified experimental results for each non-uniform rhombohedral experiment.

In regard to dominating forces in the non-uniform rhombohedral arrangement, drainage flowrates (42 ml/hr and 0.5 ml/hr) and fluid properties (Table 2) were again the same as those in the

uniform and non-uniform cubic experiments, indicating that flow regimes and dominating forces remain predictable via the Lenormand diagram (Figure 18). However, observations of distinct viscous fingering post-drainage in the non-uniform rhombohedral arrangement are again less visible compared to those observed in the uniform cubic arrangement (Figure 30). This is attributed to both the high-porosity zone essentially restricting long viscous fingered flow to occur and the new geometry introduced by the rhombohedral packing, as distinct viscous finger flow is more difficult to see due to the more tortuous flow paths required for the nonwetting phase to make its way through the rhombohedral bead pack.

Fast drainages (42ml/hr), once again, result in a larger amount of nonwetting phase post-drainage (S_I) compared to slow drainages (0.5ml/hr) (Figure 31 and Table 9). However, when analyzed with subsequent imbibition phases (S_r), slow drainages (0.5ml/hr) are, once again, more efficient than fast drainages (42 ml/hr), which was observed in uniform cubic experiments but not in non-uniform cubic experiments. This consistency, with the uniform cubic bead pack, in observed nonwetting phase trapping efficiency trend is attributed to the reduced amount of high-porosity zones present in the non-uniform rhombohedral bead pack, in comparison to the non-uniform cubic arrangement. Additionally, the initial Euler numbers observed in the non-uniform rhombohedral arrangement follows those observed in both the uniform and non-uniform cubic arrangement, more disconnect of the nonwetting phase is present after slow drainages compared to fast drainages (Figure 32 and Table 10).

The observed increase in nonwetting phase trapping efficiency after slow drainages (0.5 ml/hr) in both the uniform cubic and non-uniform rhombohedral but not in the non-uniform cubic, speaks

to the influence of geometry and system heterogeneity on nonwetting phase trapping efficiency. Uniform cubic and non-uniform rhombohedral arrangements, which introduce both a difference in geometry and uniformity, both follow the same trends as far as flowrate, post-drainage topology, and trapping efficiency. However, non-uniform cubic arrangement only follows the same trends, in regard to flowrates and topology, through the end of drainage (S_I). The alteration in trend, between non-uniform cubic and uniform cubic and non-uniform rhombohedral, is observed post-imbibition (S_r). This can be attributed to the higher-non-uniformity of the non-uniform cubic bead pack (more high-porosity zones), in comparison to the lesser-non-uniformity of the non-uniform rhombohedral bead pack (less high-porosity zones). While slow drainage rates (0.5 ml/hr) and more disconnect of the nonwetting phase post-drainage (higher initial Euler numbers) was observed to be most conducive to trapping efficiency in uniform and less-non-uniform bead packs regardless of geometry, the highly-non-uniform arrangements indicate that high-porosity zones present within a system must also be considered in overall trapping efficiency of the nonwetting phase (S_r/S_I).

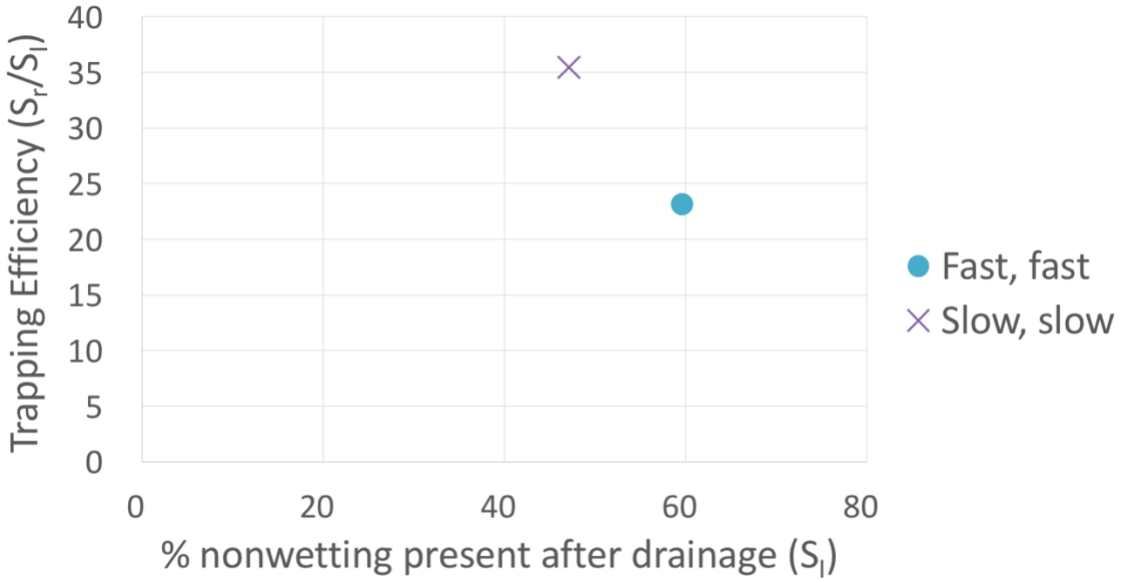

Figure 31: Trapping efficiency (S_r/S_I) for non-uniform rhombohedral experiments.

Table 9: Experimental flowrates and percent nonwetting phase trapped after drainage and imbibition for non-uniform rhombohedral arrangement

Experiment	Drainage Rate (ml/hr)	% Trapped after drainage (S_I)	Imbibition Rate (ml/hr)	% Trapped after imbibition (S_r)	Trapping Efficiency (S_r/S_I)
Fast, fast	**42**	**60**	**42**	**14**	**23**
Slow, slow	**0.5**	**47**	**0.5**	**17**	**36**

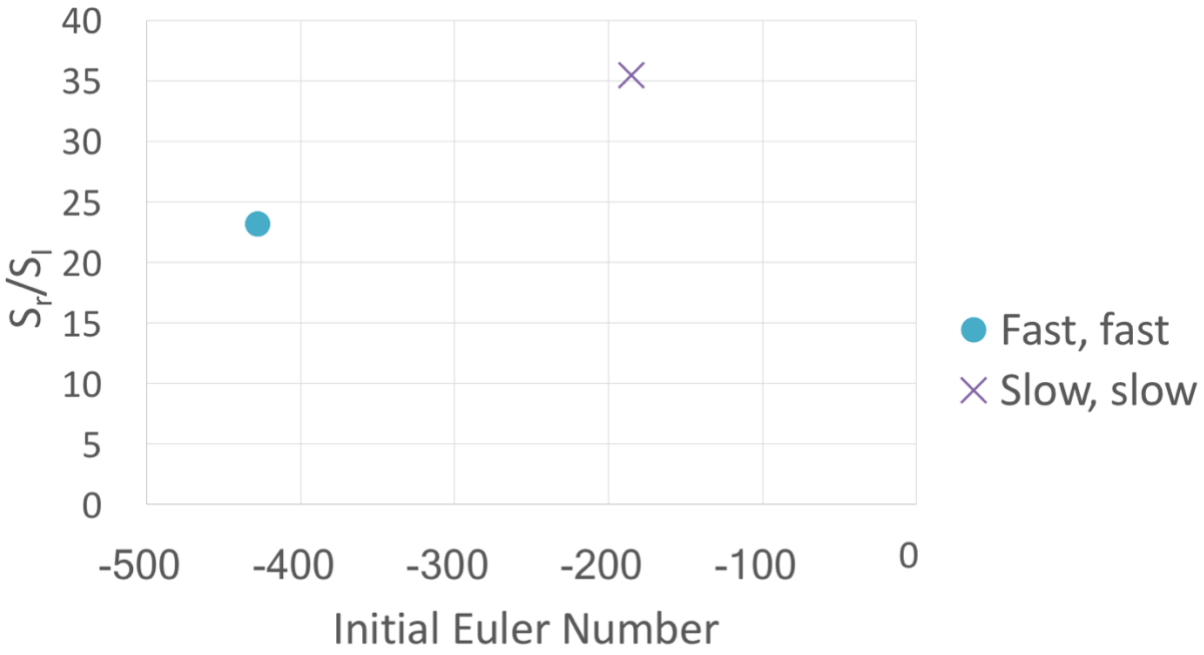

Figure 32: Trapping efficiency as a function of initial Euler number in a non-uniform rhombohedral arrangement.

Table 10: Connectivity values after drainage for a non-uniform rhombohedral arrangement.

Experiments	**Initial Euler Number**	**% nonwetting phase trapped (S_r/S_I)**
Slow, slow		
Slow Drainage	-185	36
Fast, fast		
Fast Drainage	-428	23

Chapter 6: Conclusions

This work examined the independent and combined effects of drainage and imbibition flowrate on nonwetting phase capillary trapping in a two-phase, porous medium system. This research explored the findings and theory of Herring et al. (2013) and provides complementary evidence in support of our ability to design the injection process to maximize trapping. A uniform system of cubic arrangement and non-uniform systems of both cubic and rhombohedral arrangements were examined in order to analyze and compare the nonwetting phase trapping trends between uniform and non-uniform porous media. The unique system set-up, presented in this work, allowed experiments to be performed in 3-D printed bead packs (of different arrangements) and quantified with 2-D images. A summary of the main research findings analyzing dominating forces, flowrate, and topology's influence on nonwetting phase trapping efficiency, through uniform cubic, non-uniform cubic, and non-uniform rhombohedral arrangements are presented here. In the following, drainage refers to CO_2 injection, while imbibition represents the return-flow of brine:

6.1 Uniform cubic arrangement

- Slower drainage flowrates, regardless of the subsequent imbibition flowrate, resulted in the largest amount of nonwetting phase ultimately trapped in comparison to higher drainage flowrates.
- Slow drainages correspond to a capillary dominated flow regime and greater disconnect of the nonwetting phase post-drainage, both of which are found to be conducive to nonwetting phase trapping.

6.2 Non-uniform cubic arrangement

While the observed trends in flowrate and topology at the end of drainage (S_I) are in agreement with experimental observations of the uniform cubic arrangement, the trend is altered post-imbibition (S_I). This is due to the larger amount of nonwetting phase brought in during fast drainage, compared to slow drainage. We observe that a portion of this introduced nonwetting phase is being trapped by the non-uniformities (system heterogeneity) present.

6.3 Non-uniform rhombohedral arrangement

The observed trapping efficiency trends of the non-uniform rhombohedral arrangement are in agreement with those observed in the uniform cubic arrangement throughout both drainage and imbibition. This is due to the reduced number of high-porosity zones (system heterogeneity) present in the non-uniform rhombohedral compared to the amount in the non-uniform cubic. Additionally, it is observed that a change in geometry (cubic to rhombohedral) is less influential on trapping efficiency than the presence of high-porosity zones in a system.

It is therefore suggested that drainage flowrate ($scCO_2$ injection) and a system's uniformity be considered in order to favorably influence trapping efficiency in $scCO_2$ injection schemes.

Bibliography

Allen, M.R., et al., 2018: Framing and Context. In: *Global Warming of 1.5°C. An IPCC Special Report on the impacts of global warming of 1.5°C above pre-industrial levels and related global greenhouse gas emission pathways, in the context of strengthening the global response to the threat of climate change, sustainable development, and efforts to eradicate poverty* [Masson-Delmotte, V., P. Zhai, H.-O. Pörtner, D. Roberts, J. Skea, P.R. Shukla, A. Pirani, W. Moufouma-Okia, C. Péan, R. Pidcock, S. Connors, J.B.R. Matthews, Y. Chen, X. Zhou, M.I. Gomis, E. Lonnoy, T. Maycock, M. Tignor, and T. Waterfield (eds.)]. In Press.

Al-Raoush, R. I. ;Willson, C. S. (2013). A Pore-scale Investigation of a Multiphase Porous Media System. J. Contam. Hydrol., 77(1–2).

Anderson, W. G. (1987). Wettability Literature Survey- Part 4: Effects of Wettability on Capillary Pressure. Journal of Petroleum Technology, 39(10), 1283–1300. https://doi.org/10.2118/15271-PA

Andersson, Herring, Schlüter, & Wildenschild. (2018). Defining a novel pore-body to pore-throat "Morphological Aspect Ratio" that scales with residual non-wetting phase capillary trapping in porous media. Advances in Water Resources, 122, 251–262. https://doi.org/10.1016/j.advwatres.2018.10.009

Bachu, S. (2003). Screening and ranking of sedimentary basins for sequestration of CO 2 in geological media in response to climate change. Environmental Geology, 44(3), 277–289. https://doi.org/10.1007/s00254-003-0762-9

Bachu, S., & Bennion, B. (2008). Effects of in-situ conditions on relative permeability characteristics of CO 2 -brine systems. Environmental Geology, 54(8), 1707–1722. https://doi.org/10.1007/s00254-007-0946-9

Blunt, & Scher. (1995). Pore-level modeling of wetting. Physical Review. E, Statistical Physics, Plasmas, Fluids, and Related Interdisciplinary Topics, 52(6), 6387–6403. https://doi.org/10.1103/PhysRevE.52.6387

Chatzis, I., & Morrow, N. R. (1984). Correlation of capillary number relationships for sandstone. SPEJ, Soc. Pet. Eng. J., 24(5).

Cao, Dai, & Jung. (2016). Supercritical CO2 and brine displacement in geological carbon sequestration: Micromodel and pore network simulation studies. International Journal of Greenhouse Gas Control, 44, 104–114. https://doi.org/10.1016/j.ijggc.2015.11.026

Dullien, F. A. L. and Howard Brenner (1992). Capillarity in Porous Media. *Porous Media Fluid Transport and Pore Structure.* Academic Press, Inc, 1992, pp. 133–137.

Garcia, S., Kaminska, S., & M. Mercedes Maroto-Valer. (2010). Underground carbon dioxide storage in saline formations. Proceedings of the ICE - Waste and Resource Management, 163(2), 77–88. https://doi.org/10.1680/warm.2010.163.2.77

Herring, A. L., Harper, E. J., Andersson, L., Sheppard, A., Bay, B. K., & Wildenschild, D. (2013). Effect of fluid topology on residual nonwetting phase trapping: Implications for geologic CO2 sequestration. Advances in Water Resources, 62, 47–58. https://doi.org/10.1016/j.advwatres.2013.09.015

IPCC. Special report on carbon dioxide capture and storage. New York: Cambridge University Press; 2005 (ISBN:92-9169-1190-4).

Joekar-Niasar, V., & Hassanizadeh, S. M. (2012). Analysis of Fundamentals of Two-Phase Flow in Porous Media Using Dynamic Pore-Network Models: A Review. Critical Reviews in Environmental Science and Technology, 42(18), 1895–1976. https://doi.org/10.1080/10643389.2011.574101

Kimbrel, Herring, Armstrong, Lunati, Bay, & Wildenschild. (2015). Experimental characterization of nonwetting phase trapping and implications for geologic CO2 sequestration. International Journal of Greenhouse Gas Control, 42, 1–15. https://doi.org/10.1016/j.ijggc.2015.07.011

Knapik, E., Janiga, D., Wojnarowski, P., & Stopa, J. (2015). The role of capillary trapping during geologic CO 2 sequestration. AGH Drilling, Oil, Gas, 32(4). https://doi.org/10.7494/drill.2015.32.4.657

Krevor, S. C. M., Pini, R., Li, B., & Benson, S. M. (2011). Capillary heterogeneity trapping of CO2 in a sandstone rock at reservoir conditions. Geophysical Research Letters, 38(15), n/a-n/a. https://doi.org/10.1029/2011GL048239

Lenormand, R., Touboul, E., & Zarcone, C. (1988). Numerical models and experiments on immiscible displacements in porous media. Journal of Fluid Mechanics, 189, 165–187. https://doi.org/10.1017/S0022112088000953

Leung, Dennis Y.C., Caramanna, Giorgio, & Maroto-Valer, M. Mercedes. (2014). An overview of current status of carbon dioxide capture and storage technologies. Renewable and Sustainable Energy Reviews, 39.

Morrow, N. R., Chatzis, I., & Taber, J. J. (1988). Entrapment and Mobilization of Residual Oil in Bead Packs. SPE Reservoir Engineering, 3(3), 927–934. https://doi.org/10.2118/14423-PA

Nguyen, Sheppard, Knackstedt, & Val Pinczewski. (2006). The effect of displacement rate on imbibition relative permeability and residual saturation. Journal of Petroleum Science and Engineering, 52(1), 54–70. https://doi.org/10.1016/j.petrol.2006.03.020

Otsu, N. (1979). A Threshold Selection Method from Gray-Level Histograms. IEEE Transactions on Systems, Man, and Cybernetics, 9(1), 62–66. https://doi.org/10.1109/TSMC.1979.4310076

Roof, J. G. (1970). Snap-Off of Oil Droplets in Water-Wet Pores. Society of Petroleum Engineers Journal, 10(1), 85–90. https://doi.org/10.2118/2504-PA

Tanino, Y., & Blunt, M. J. (2012). Capillary trapping in sandstones and carbonates: Dependence on pore structure. Water Resources Research, 48(8), n/a-n/a. https://doi.org/10.1029/2011WR011712

Wildenschild, D. S., Adrian P. (2013). X-ray imaging and analysis techniques for quantifying pore-scale structure and processes in subsurface porous medium systems. Adv. Water Resour., 51(1), 217–246. https://doi.org/10.1016/j.advwatres.2012.07.018

Wilcox, J, et al. (2017). Assessment of reasonable opportunities for direct air capture. Environmental Research Letters, 12(6), 065001/1-065001/7.

Wilson, B., et al. (2016). An Evaluation of Subsurface Microbial Activity Conditional to Subsurface Temperature, Porosity, and Permeability at North American Carbon Sequestration Sites. National Energy Technology Laboratory, doi:10.2172/1327812.

Zhang, C., Oostrom, M., Wietsma, T. W., Grate, J. W., & Warner, M. G. (2011). Influence of Viscous and Capillary Forces on Immiscible Fluid Displacement: Pore-Scale Experimental Study in a Water-Wet Micromodel Demonstrating Viscous and Capillary Fingering. Energy and Fuels, 25:3493-3505, 25(8), 3493-3505-3493–3505. https://doi.org/10.1021/ef101732k